# UC Berkeley
## UC Berkeley Previously Published Works

**Title**
Phillipsite and Al-tobermorite mineral cements produced through low-temperature water-rock reactions in Roman marine concrete

**Permalink**
https://escholarship.org/uc/item/881113j7

**Journal**
American Mineralogist, 102(7)

**ISSN**
0003-004X

**Authors**
Jackson, Marie D
Mulcahy, Sean R
Chen, Heng
et al.

**Publication Date**
2017-07-01

**DOI**
10.2138/am-2017-5993ccby

Peer reviewed

# Phillipsite and Al-tobermorite mineral cements produced through low-temperature water-rock reactions in Roman marine concrete⌾

**Marie D. Jackson[1,*], Sean R. Mulcahy[2], Heng Chen[3], Yao Li[4], Qinfei Li[5], Piergiulio Cappelletti[6], and Hans-Rudolf Wenk[7]**

[1]Department of Geology and Geophysics, University of Utah, Salt Lake City, Utah 84112, U.S.A.
[2]Geology Department, Western Washington University, Bellingham, Washington 98225, U.S.A.
[3]School of Materials Science and Engineering, Southeast University, Nanjing 211189, People's Republic of China
[4]Center for Advancing Materials Performance from the Nanoscale (CAMP-Nano), Xi'an Jiaotong University, Xi'an 710049,
People's Republic of China
[5]School of Transportation Science and Engineering, Harbin Institute of Technology, Harbin 150090, People's Republic of China
[6]Dipartimento di Scienze della Terra, dell'Ambiente e delle Risorse (DiSTAR), Università degli Studi di Napoli Federico II, Naples I-80134,
Italy
[7]Department of Earth and Planetary Sciences, University of California, Berkeley, California 94720, U.S.A.

## Abstract

Pozzolanic reaction of volcanic ash with hydrated lime is thought to dominate the cementing fabric and durability of 2000-year-old Roman harbor concrete. Pliny the Elder, however, in first century CE emphasized rock-like cementitious processes involving volcanic ash (*pulvis*) "that as soon as it comes into contact with the waves of the sea and is submerged becomes a single stone mass (*fierem unum lapidem*), impregnable to the waves and every day stronger" (*Naturalis Historia* 35.166). Pozzolanic crystallization of Al-tobermorite, a rare, hydrothermal, calcium-silicate-hydrate mineral with cation exchange capabilities, has been previously recognized in relict lime clasts of the concrete. Synchrotron-based X-ray microdiffraction maps of cementitious microstructures in *Baianus Sinus* and *Portus Neronis* submarine breakwaters and a *Portus Cosanus* subaerial pier now reveal that Al-tobermorite also occurs in the leached perimeters of feldspar fragments, zeolitized pumice vesicles, and *in situ* phillipsite fabrics in relict pores. Production of alkaline pore fluids through dissolution-precipitation, cation-exchange and/or carbonation reactions with Campi Flegrei ash components, similar to processes in altered trachytic and basaltic tuffs, created multiple pathways to post-pozzolanic phillipsite and Al-tobermorite crystallization at ambient seawater and surface temperatures. Long-term chemical resilience of the concrete evidently relied on water-rock interactions, as Pliny the Elder inferred. Raman spectroscopic analyses of *Baianus Sinus* Al-tobermorite in diverse microstructural environments indicate a cross-linked structure with $Al^{3+}$ substitution for $Si^{4+}$ in $Q^3$ tetrahedral sites, and suggest coupled $[Al^{3+}+Na^+]$ substitution and potential for cation exchange. The mineral fabrics provide a geo-archaeological prototype for developing cementitious processes through low-temperature rock-fluid interactions, subsequent to an initial phase of reaction with lime that defines the activity of natural pozzolans. These processes have relevance to carbonation reactions in storage reservoirs for $CO_2$ in pyroclastic rocks, production of alkali-activated mineral cements in maritime concretes, and regenerative cementitious resilience in waste encapsulations using natural volcanic pozzolans.

**Keywords:** Phillipsite, Al-tobermorite, Roman concrete, natural pozzolan, water-rock reaction

## Introduction

Roman marine concrete structures, composed of a volcanic ash-hydrated lime mortar that binds conglomeratic tuff or carbonate rock aggregate (*caementa*), have remained intact and coherent for 2000 yr, either fully immersed in seawater or partially immersed in shoreline environments (Brandon et al. 2014). The extraordinary longevity of the concrete seems to result from the long-term durability of poorly crystalline, calcium-aluminum-silicate-hydrate (C-A-S-H binder) in the cementing matrix of the mortar (Jackson et al. 2013a), the sequestration of chloride and sulfate ions in discrete crystalline microstructures (Jackson et al. 2012), and, as reported here, pervasive crystallization of zeolite

and Al-tobermorite mineral cements in pumice clasts, dissolved feldspar crystal fragments, and relict voids of the cementing matrix (Figs. 1f, 1g, 1h, and 1j).

The mortar of Roman marine concrete is considered the prototype of modern concretes that partially replace Portland cement with natural pozzolan to reduce $CO_2$ emissions and produce resilient C-A-S-H binder (Snellings et al. 2012). Ancient Roman concretes also have C-A-S-H binder, but it was produced through reaction of seawater, lime (CaO) calcined from limestone, and zeolitized volcanic ash, mainly from Campi Flegrei volcano (Fig. 2) (Stanislao et al. 2011; Jackson et al. 2013a, 2014). C-A-S-H is the poorly crystalline analog of Al-tobermorite, a rare, layered, calcium-silicate hydrate mineral composed of aluminosilicate chains bounded by an interlayer region and a calcium oxide sheet (e.g., Komarneni and Roy 1983; Taylor
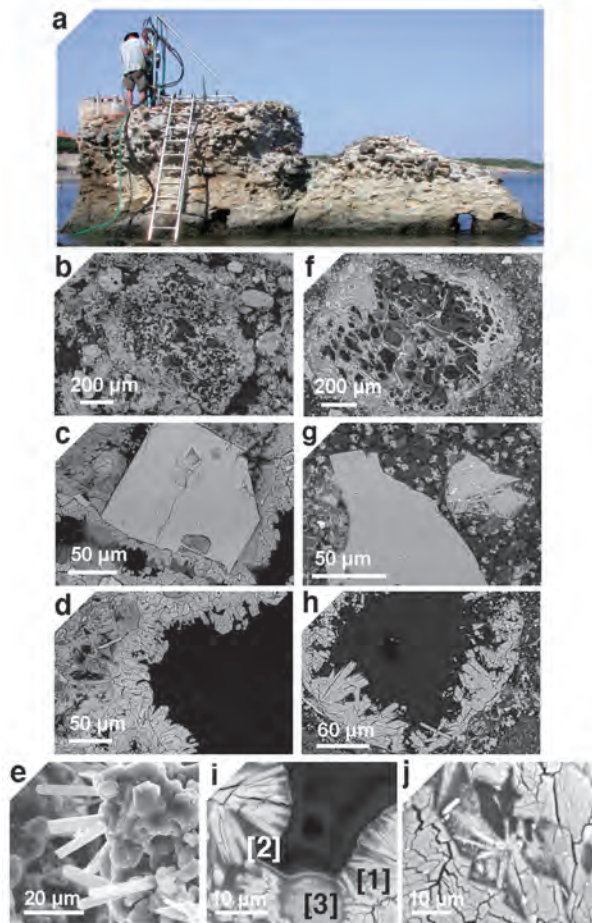
**Figure 1.** Authigenic mineral textures in tuff deposits and Roman marine mortar. Scanning electron microscopy backscattered electron (SEM-BSE) images. (**a**) *Portus Cosanus* pier, Orbetello, Italy (credit, J.P. Oleson) (Fig. 2). (**b**) Bacoli tuff (BT), pumice clast. (**c** and **d**) Neapolitan Yellow Tuff (NYT), dissolving alkali feldspar, phillipsite, and chabazite textures. (**e**) Surtsey tuff, Iceland 1979 drill core, dissolving phillipsite and associated Al-tobermorite, 37.0 m, 100 °C (credit, J.G. Moore). (**f**) *Portus Cosanus*, pumice clast with dissolved glass. (**g**) *Portus Neronis*, Anzio, Italy, dissolving alkali feldspar (see also Fig. 5). (**h**) *Portus Cosanus*, phillipsite textures. (**i**) *Portus Cosanus*, dissolving Campi Flegrei phillipsite [1], pozzolanic C-A-S-H binder [2] and Al-tobermorite [3] (see Fig. 7i for X-ray microdiffraction patterns). (**j**) *Portus Baianus*, Pozzuoli, Italy, dissolving *in situ* phillipsite and associated Al-tobermorite (Fig. 9).

1992; Richardson 2014; Myers et al. 2015a). Al-tobermorite does not occur in conventional concretes but occurs routinely in the relict lime clasts of Roman marine concrete (Vola et al. 2011; Jackson 2014) and, occasionally, in hydrothermally altered volcanic rocks (Figs. 3 and 4). Al-tobermorite also occurs as an alteration product at the cement–rock interface of toxic and nuclear waste repositories (e.g., Gaucher and Blanc 2006; Lalan et al. 2016). Tobermorite group minerals have a basal interlayer spacing of ~11 Å and an orthorhombic sub-cell symmetry with the general formula, $Ca_{4+x}(Al_ySi_{6-y})O_{15+2x-y} \cdot 5H_2O$, where x = 1 and y = 2 (Biagioni et al. 2015). Most geological occurrences have



**Figure 2.** Ancient Roman concrete harbors and ROMACONS project drill sites, green circles: 1 = *Portus Cosanus*, 2 = *Portus Traianus*, 3 = *Portus Neronis*, 4 = *Baianus Sinus*. Volcanic districts, red triangles (after Jackson et al. 2013a).

$Al^{3+}$ substitution for $Si^{4+}$ in tetrahedral sites, and the generalized mineral formula, $\{[Ca_4(Si_{5.5}Al_{0.5}O_{17}H_2)]Ca_{0.2} \cdot Na_{0.1} \cdot 4H_2O$ (Taylor 1992)\}, contains sodium and potassium as interlayer cations (Figs. 3b and 4b). Substitution of $Al^{3+}$ for $Si^{4+}$ in Al-tobermorite synthesized at 80–240 °C also produces ion-exchange behavior for certain radionuclides and heavy metals as interlayer cations (Komarneni and Roy 1983; Komarneni et al. 1987; Trotignon et al. 2007; Coleman et al. 2014). The crystals could prove useful in cementitious barriers and for nuclear and hazardous waste treatment and disposal if they could be produced in sufficient quantities at low temperature and, potentially, through regenerative, *in situ* cementitious processes over long periods of time.

Natural pozzolans are siliceous and/or aluminous earth materials: volcanic glass, zeolite minerals, opaline chert, and diatomaceous earths. They form part of a broader class of supplemental cementitious materials (SCMs), such as fly ash, a waste product from coal-fired power plants, now incorporated in environmentally friendly cement and concrete technologies (Lothenbach et al. 2011). Pozzolans are defined as materials "which, in themselves, possess little or no cementitious value but which will, in finely divided form and in the presence of water, react chemically with calcium hydroxide [portlandite, $Ca(OH)_2$] to form compounds possessing cementitious properties" (Mehta 1987). Pozzolanic activity is measured through various chemical tests, which determine a material's reactivity with portlandite and the rate at which it binds $Ca(OH)_2$ in the presence of water (Massazza 2004), as well as mechanical tests, which measure compressive strength over 28 days, for example, as a means to predict long-term performance (ASTM-C618 2015). When finely

ground these natural or artificial pozzolanic materials are mixed with Portland cement to produce a blended cement paste that binds largely inert sand- and gravel-sized aggregates. Blended cement pastes generally have a more refined pore structure, increased chemical resistance to the ingress and deleterious action of aggressive solutions, such as seawater, and to expansive alkali-silica reactions associated with reactive aggregates that degrade concretes worldwide (e.g., Massazza 2004; Mehta and Monteiro 2015, p. 169–172), as compared with ordinary Portland cement paste. Although reliable large-scale production of concretes with natural pozzolans has not been fully mastered relative to those

with SCMs such as fly ash, recent reductions in fly ash production and availability are now driving new interest in volcanic rock pozzolans (e.g., Celik et al. 2014; Cai et al. 2016).

The life cycle of Roman harbor concretes structures is about two orders of magnitude greater than Portland-type cement seawater concretes. Cement-based concretes are designed to hydrate quickly and maintain durability through a general absence of long-term cementitious evolution or solubility. In maritime environments, however, the concrete commonly begins to decay after a few decades due, in part, to corrosion of steel reinforcement (Mehta 1990). The steel reinforcement counteracts the relative low tensile
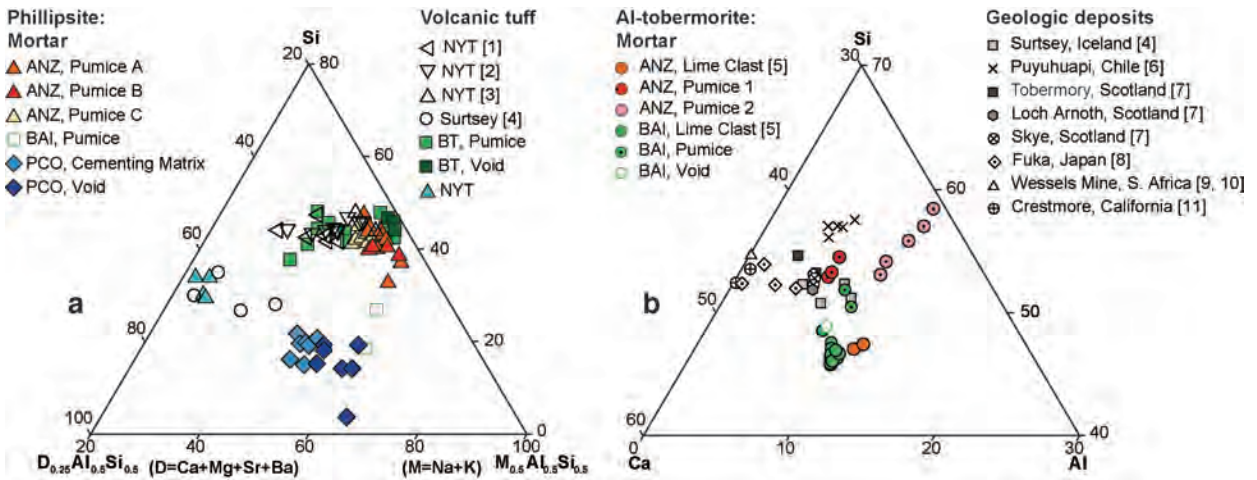


**FIGURE 3.** Compositions of phillipsite and Al-tobermorite in Roman marine mortars and geologic deposits. Electron probe microanalyses (EPMA), as molecular proportions (Tables 1, 2, and S1). (**a**) Phillipsite, published compositions from [1] Passaglia et al. 1990; [2] de Gennaro et al. 2000; [3] Gatta et al. 2010; [4] Jakobsson and Moore 1986. (**b**) Al-tobermorite, various geologic deposits (after [5] Jackson et al. 2013a). [6] Aguirre et al. 1998; Claringbull and Hey 1952; [7] Livingstone 1988; [8] Henmi and Kusachi 1992; [9,10] Hoffman and Armbuster 1997; Merlino et al. 2001; [11] Mitsuda and Taylor 1978. Roman crystals have Al/(Si+Al) = 0.10–0.16 and Ca/(Si+Al) = 0.45–0.69. Sodium and potassium range from 1–3 wt%. ANZ = *Portus Neronis*; BAI = *Baianus Sinus*; PCO = *Portus Cosanus*; NYT = Neapolitan Yellow Tuff; BT = Bacoli Tuff.
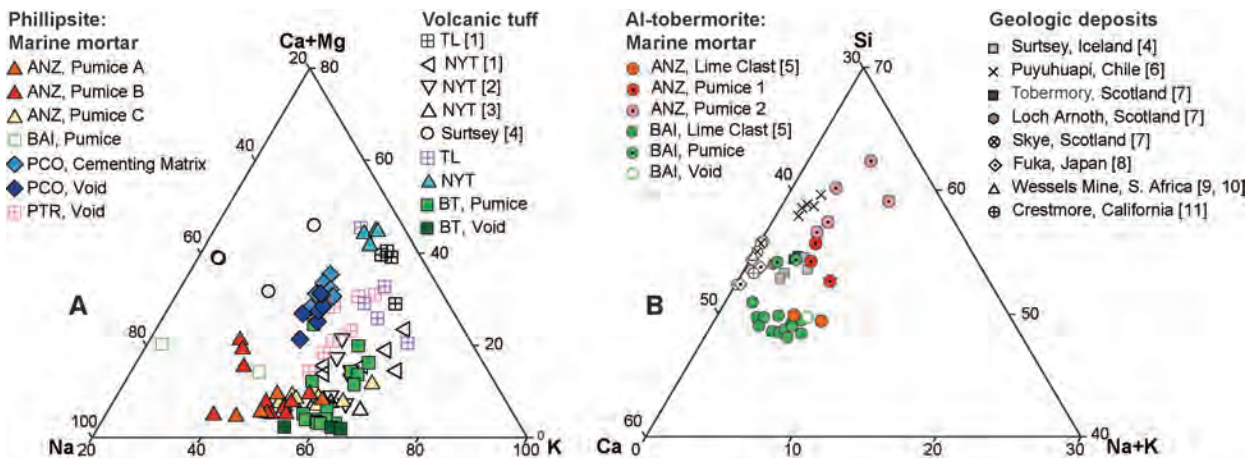


**FIGURE 4.** Compositions of phillipsite and Al-tobermorite in Roman marine mortars and geologic deposits. Electron probe microanalyses (EPMA), as molecular proportions (Tables 1, 2, and S1). (**a**) Phillipsite, Ca+Mg-Na-K, see Figure 3 for references to published compositions. Phillipsite compositions in relict voids of *Portus Traianus* mortar, Ostia, Italy, are similar to phillipsite in Tufo Lionato (TL) tuff coarse aggregate, erupted at 366 ± 5 ka from Alban Hills volcano (Marra et al. 2009). (**b**) Al-tobermorite, Si-Ca-Na+K, various geologic deposits (after [5] Jackson et al. 2013a). PTR = *Portus Traianus*. The most silicic compositions are similar to Al-tobermorite in Surtsey basaltic tuff, Iceland (Jakobsson and Moore 1986). Tobermorite is not observed in NYT, BT, and TL, but occurs in deeper Campi Flegrei deposits (Vanorio and Kanitpanyacharoen 2015).

strength and ductility of the concrete and, therefore, is a structural requirement. Although concretes with pozzolanic blended cements generally have reduced calcium hydroxide content relative to conventional concretes with Portland cement alone, the presence of calcium hydroxide as free portlandite may persist for long periods of time depending on the weight percent addition of SCM (Goñl et al. 2005). Highly alkaline pore solutions may thus persist indefinitely and, in the absence of chloride ions in solution, the protective film on steel remains stable as long as solution pH ≥ 11.5 (Mehta and Monteiro 2015, p. 179). Interaction of seawater with marine concrete corrodes steel, however, and also may produce expansive reactions with calcium hydroxide (Massazza 1985). By contrast, portlandite is rapidly consumed in Roman pyroclastic rock concrete reproductions, and there is no steel reinforcement in the ancient structures; the volcanic ash mortars show greater ductility and bind a conglomeratic rock framework that reinforces the concrete at the structural scale (Brune et al. 2013; Jackson 2014; Jackson et al. 2014). Roman marine concrete structures throughout the Mediterranean region contain reactive, alkaline, fine sand- to gravel-sized, pumiceous ash aggregate, commonly with zeolite surface coatings and the massive harbor structures have been left open to seawater ingress for two millennia. Although pozzolanic processes in the ancient concrete have been described (Jackson et al. 2013a), little is known about post-pozzolanic cementitious processes that could benefit chemical resilience long after calcium hydroxide was fully consumed through pozzolanic reaction with the volcanic ash aggregate.

Vitruvius, a Roman architect and engineer writing about 30 BCE, described this pozzolanic reaction and the "latent" heat released when tuff, pumiceous ash, and lime (CaO) (*tofus*, *pulvis*, and *calyx*) from the Campi Flegrei and Vesuvius volcanic districts "come into one mixture and suddenly take up water and cohere together" (*de Architectura* 2.6.1–4) (Appendix Table 1). An adiabatic model of exothermic heat evolved during hydration of lime and production of pozzolanic C-A-S-H binder in a 10 m$^2$ by 6 m tall *Baianus Sinus* breakwater in the Bay of Pozzuoli, Italy (Fig. 2, location 4), indicates that elevated temperatures, 65–95 °C, persisted for 2–3 yr (Jackson et al. 2013a). In partially dissolved relict lime clasts, crystallization of Al-tobermorite associated with C-A-S-H likely accompanied this pozzolanic phase of reaction, which apparently terminated early in the history of the maritime concrete structures. In a Roman concrete breakwater reproduction, for example, portlandite was fully consumed after 5 yr of hydration in seawater (Oleson et al. 2006; Gotti et al. 2008; Jackson 2014), similar to other experimental seawater concretes with volcanic ash aggregates (Massazza 1985).

Roman natural scientists, Seneca (4 BCE–64 CE) and Pliny the Elder (23–79 CE), used geologic analogs to explain the longer term cohesion of the maritime concretes, beyond that observed by Vitruvius (Appendix Table 1). Pliny called upon the natural capacity of alkaline volcanic ash to react with water, quickly promote lithification, and, by analogy, produce rock-like qualities of endurance in marine concrete: "as soon as [volcanic ash (*pulvis*)] comes into contact with the waves of the sea and is submerged becomes a single stone mass (*fierem unum lapidem*), impregnable to the waves and every day stronger" (*Naturalis Historia* 35.166). The volcanic rock-fluid interactions inferred by Seneca and Pliny are recorded by authigenic mineral textures in the pumiceous

mortar fabric of submarine and subaerial marine concrete structures. These occur in the dissolved perimeter of feldspar crystals (Fig. 1g), pumice vesicles (Fig. 1h), and pores of the cementing matrix (Fig. 1i).

To investigate these rock-like cementitious processes we compare electron probe microanalysis compositions of phillipsite, a potassic, sodic, and/or calcic zeolite, and Al-tobermorite that formed in volcanic deposits with analogous crystals that formed in the marine concrete (Figs. 3 and 4). We map Roman cementitious microstructures with synchroton-based X-ray microdiffraction (Figs. 5–9) to describe *in situ* zeolite and Al-tobermorite textures in the *Portus Cosanus* subaerial pier and the *Baianus Sinus* and *Portus Neronis* submarine breakwaters (Fig. 2). We then use Raman spectroscopy to identify bonding environments in *Baianus Sinus* Al-tobermorite from various crystallization environments. Comparison of these spectra with those previously determined for ideal tobermorite give a qualitative measure of the role of aluminum in a cross-linked crystal structure (Figs. 10–12). The integrated results provide new insights into the low temperature crystallization and stability of phillipsite and Al-tobermorite in alkaline aqueous environments and illustrate the beneficial role of authigenic mineral cycling in construction materials with natural volcanic pozzolan over very long service lives.

## MATERIALS AND ANALYTICAL METHODS

Roman harbor concrete structures were constructed from about 55 BCE to 115 CE, and cored by the ROMACONS drilling program from 2002 to 2006 (Brandon et al. 2014). The conglomeratic concrete cores contain about 40–45 vol% zeolitized tuff coarse aggregate, and 55–60 vol% pumiceous volcanic ash-hydrated lime mortar. The marine concrete is exposed sub-aerially at *Portus Cosanus* (drill core PCO.03.01), Orbetello, (42.4079° N, 11.2933° E), and submerged in seawater at *Baianus Sinus* (BAI.06.03), Bay of Pozzuoli, (40.8228° N, 14.0885° E), *Portus Neronis* (ANZ.02.01), Anzio, (41.4432° N, 12.6314° E) and *Portus Traianus* (PTR.02.02), Ostia (41.7785° N, 12.2520° E). The BT sample comes from an unidentified quarry near Fondi di Baia, at about 40.80° N, 14.07° E; the NYT samples come from outcrops in Naples at 40.89° N, 14.18° E.

### Electron probe microanalysis (EPMA)

Samples were analyzed with a Cameca SX-51 electron microprobe equipped with five wavelength-dispersive spectrometers using a 15 keV accelerating voltage, a 10 nA beam current, and a 1–2 μm beam diameter. Counting time was 10 s on peak and background for all elements. Major element compositions of phillipsite and clusters of 1–5 μm Al-tobermorite were acquired from polished thin sections of tuffs and mortars prepared according to hydrophobic specifications. New determinations of phillipsite compositions in Campi Flegrei Bacoli Tuff (BT) and Neapolitan Yellow Tuff (NYT) deposits and of phillipsite and Al-tobermorite compositions in the marine mortars are compared with previously published compositions (Figs. 3 and 4; Tables 1, 2, and Supplemental[1] Table S1). To account for potential Na and K loss and/or Si and Al gain, a time dependent intensity calibration was also applied to these elements using the software Probe for EPMA (e.g., Meier et al. 2011). Oxygen and water content were calculated by stoichiometry. Uncertainties in the weight percent oxides were determined by counting statistics and propagated through the calculation of formula units (Giaramita and Day 1990). The fine grain size of Al-tobermorite contributed to lower wt% oxide measurements. Analyses with wt% oxide totals <80 (with H$_2$O calculated by stoichiometry) and low atoms per formula unit were omitted from Table 2. Areas with visible traces of calcium carbonate crystals were not analyzed. Plotting coordinates for ternary diagrams were calculated from the mineral formulas of phillipsite and Al-tobermorite. The Si-D$_{0.25}$Al$_{0.50}$Si$_{0.50}$–M$_{0.50}$Al$_{0.50}$Si$_{0.50}$ molecular proportions were calculated as
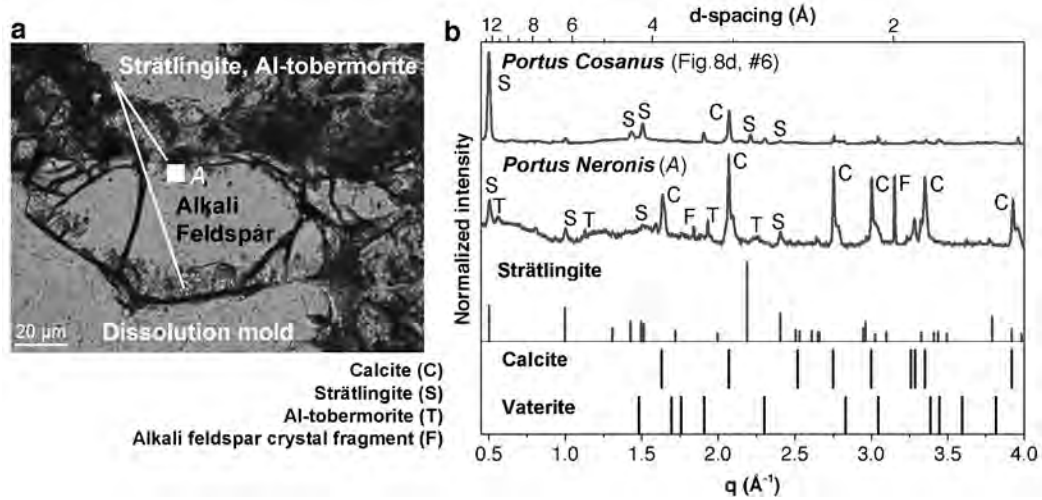
**FIGURE 5.** Dissolution of an alkali feldspar crystal fragment in *Portus Neronis* mortar and associated crystalline cementitious phases, strätlingite and Al-tobermorite, in the interfacial perimeter. (**a**) In situ dissolution produced a 100 μm² dissolution mold in the already hardened cementing matrix, petrographic image. (**b**) X-ray microdiffraction patterns for cementitious minerals in the interfacial zone of the partially dissolved alkali feldspar single crystal (F) include strätlingite (S), Al-tobermorite (T), and calcite (C). Only weak reflections of the feldspar single crystal are shown by the monochromatic X-ray beam; $q$ is calculated as $2\pi/d$-spacing.
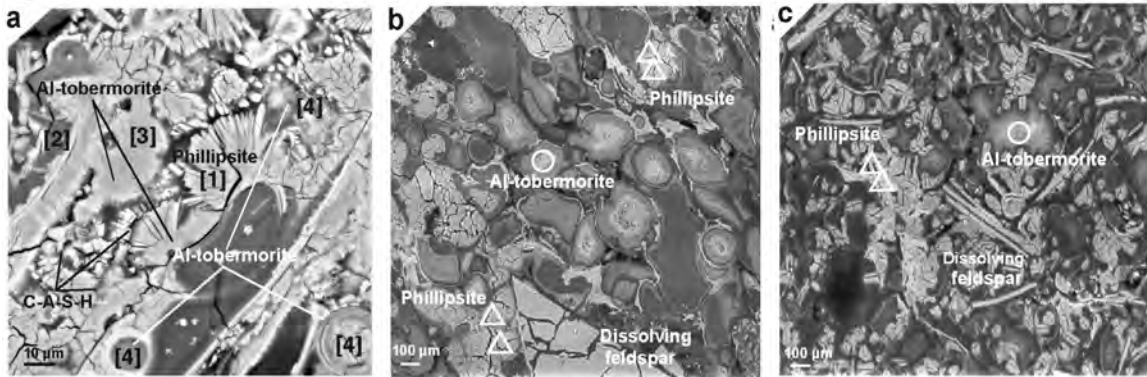


**FIGURE 6.** SEM-BSE images of Al-tobermorite and zeolite in pumice clasts. (**a**) *Portus Cosanus*, dissolving Campi Flegrei phillipsite [1], pozzolanic C-A-S-H binder [2] and Al-tobermorite [3], and later accumulations of very fine-grained Al-tobermorite [4]. (**b**) *Portus Neronis*, examples of EPMA analyses in *Portus Neronis* mortar pumice clasts, with partially dissolved alkali feldspar, relict geologic phillipsite, and associated Al-tobermorite in vesicles.

$Si = Si - Al$; $D_{0.25}Al_{0.50}Si_{0.50} = 2[2Al(Ca+Mg+Ba+Sr)]/[(Na+K) + 2(Ca+Mg+Ba+Sr)]$; $M = 2[Al(Na+K)]/[(Na+K) + 2(Ca+Mg+Ba+Sr)]$, where D and M refer to divalent and monovalent cations, respectively (Deer et al. 2004; Gatta et al. 2010). The plotting coordinates of other ternary diagrams are based on molecular proportions as defined at the apices of a given diagram.

### Synchroton-based X-ray microdiffraction

Crystalline phases in *Portus Cosanus* and *Baianus Sinus* cementitious microstructures were determined at Advanced Light Source beamline 12.3.2 at Lawrence Berkeley National Laboratory (Tamura et al. 2009) with microdiffraction and microfluoresence analyses (Figs. 5 and 7–9). Polished thin sections were prepared using superglue adhesive, studied with petrographic methods, and then detached from the glass slide by soaking in nitromethane. The 0.3 mm thick mortar slice was then mounted on adhesive tape and loaded in transmission mode into the beam, with the detector tilted at 30–39° to the incident beam. A monochromatic X-ray beam of 8 or 10 keV was focused to a $2 \times 5$ μm² diameter spot size. A Pilatus 1M area detector placed at 150 mm recorded Debye rings diffracted by crystalline phases. Debye rings at successive $d$-spacing reflections were integrated radially for 2θ, 3° up to 54°, over an arch segment around the cone of diffraction of up to 76° to create intensity vs. $d$-spacing plots. These are shown as $q = 2\pi/d$-spacing, to increase readability of low $d$-spacing reflections.

### Scanning electron microscopy (SEM)

Compositional high-resolution energy-dispersive X-ray spectroscopy (EDS) elemental maps of the same *Portus Cosanus* and *Baianus Sinus* microstructures were obtained with a Bruker Xflash 5060F Silicon Drift Detector (SDD) on a Zeiss Merlin Compact Scanning Electron Microscope (SEM) at the Bruker Laboratories in Berlin, Germany (Figs. 7 and 9). Element concentrations are displayed by quantitative mapping (QMap) in normalized mass% using the PB-ZAF quantification method. Element distributions are shown in false color display from black to blue, green, yellow to red, with the highest mass% concentration. Noise was removed by adjusting the maximum intensity threshold for each element. The analyses utilized high voltage, 8 keV, resolution of 379 nm per pixel, and 196 μs residence time (Figs. 7b and 7c), 197 nm per pixel, 88 μs (Figs. 7f and 7g), and 10 keV, 388 nm per pixel, 312 μs (Figs. 7k–7n). Backscattered (BSE) images of tuffs and mortars (Figs. 1b–d, 1f–1j, 6, 7a–7c, 8a–8c, 9a, and 9b) were acquired with the Zeiss EVOMA10 Scanning Electron Microscope at the UC Berkeley Department of Earth and Planetary Science. A secondary electron image (Fig. 1e) of Surtsey tuff from a 1979 drill core was acquired by J.G. Moore in 1979 using an ARL-EMX microprobe at the U.S. Geological Survey, Menlo Park, California.
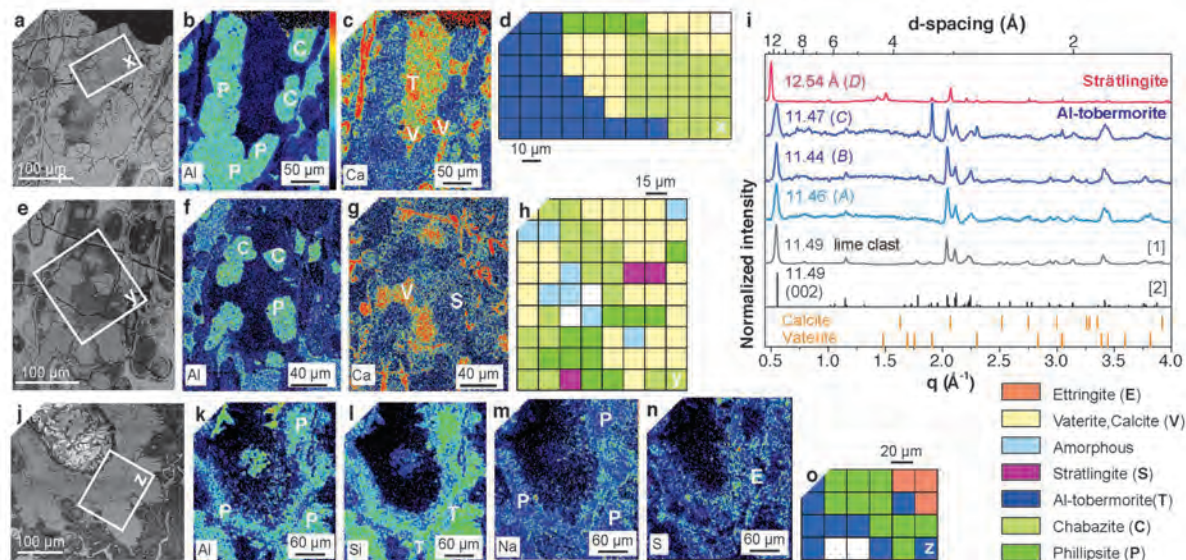
**FIGURE 7.** Comparison of microstructures showing Al-tobermorite crystallization in association with zeolite alteration. (**a–h**) *Portus Cosanus*, pumice clast. (**j–o**) *Baianus Sinus*, relict pores in the cementing matrix. SEM BSE images, energy-dispersive X-ray (SEM-EDS) spectroscopy maps, and X-ray microdiffraction maps (see Figs. 8 and 9 for details). (**i**) X-ray microdiffraction patterns, *Portus Cosanus* pumice clast: early Al-tobermorite (*A*, Fig. 1j, location [1]), later Al-tobermorite (*B*, Fig. 1j, in vesicle near [1], *C*, Fig. 8b, location 66) and strätlingite (*D*, Fig. 8d, location 06). Reference Al-tobermorite diffraction patterns from [1] Jackson et al. (2013a), *Baianus Sinus* relict lime clast, [2] Yamazaki and Toraya (2001), Al-tobermorite synthesis; SEM-EDS maps **b**, **c**, **f**, and **g** scaled to red = 20 normalized mass% at each point; SEM-EDS maps **l–p** scaled to red = maximum mass%: Al, 9.5; Si, 24.7; K, 6.7; Na, 18.6; S, 10.2; Cl, 3.7.

## Raman spectroscopy

Raman spectra obtained through a confocal microscope is correlated with crystals in cementitious microstructures previously analyzed with X-ray microdiffraction in *Baianus Sinus* relict lime clasts, pumice clasts, and relict voids (Figs. 10–12, Table 3). A JYHoriba LabRAM spectrometer at the Department of Chemical Engineering, UC Berkeley, was used in backscattering configuration, with HeNe laser (632.8 nm) excitation line, power at ~5 mW, and through an 100× confocal microscope (aperture = 0.8; laser spot size <1 μm). The spectra evaluate the nearest neighbor bonding environments of the silicate tetrahedron via oxygen corresponding to $Q^n$ [$m$ Si (or Al)], where $Q^n$ silicate tetrahedra are connected via $n$ bridging O atoms to $m$ Si$^{4+}$ (or Al$^{3+}$). Bands at 1074, 1086, etc., indicate C–O stretching in calcite and vaterite (Black et al. 2007; Wehrmeister et al. 2010). No Raman spectra exist for 11 Å Al-tobermorite and C-A-S-H in published literature. We therefore compare Roman syntheses of Al-tobermorite and C-A-S-H spectra with spectra of laboratory syntheses of 11 Å tobermorite without aluminum, geologic 11 Å tobermorite from Crestmore, California, and laboratory C-S-H with calcium/silica = 0.8 to 0.83 referenced in previous NMR studies (Kirkpatrick et al. 1997; Richardson et al. 2010; Black 2009; Jackson et al. 2013a, 2013b).

## CEMENTING FABRICS

Lithification of volcanic ash to form tuffaceous rock is one of the principal processes through which a volcano consolidates and stabilizes its deposits. Diagenetic and hydrothermal interaction of surface, ground, or seawater with volcanic ash components— glass, crystals, and lithic fragments—produces a sequence of authigenic crystalline phases that cement loose tephra to form tuff (e.g., Hay and Iijima 1968; Jakobsson and Moore 1986). In the Neapolitan Yellow Tuff (NYT), 14.9 ± 0.4 ka (Fedele et al. 2011), phillipsite and chabazite, a zeolite with more calcic compositions (de Gennaro et al. 2000), formed from alkaline hydrothermal solutions produced through interactions with volcanic glass. The crystals bind a vitric matrix, consolidate interfacial zones of pumiceous clasts, and fill relict pores and pumice vesicles; alkali feldspar crystal fragments partially dissolved and also produced

zeolite textures (Figs. 1b–d). The authigenic minerals in alkali-rich trachytic to phonolitic Campi Flegrei deposits selected by Roman engineers for marine concrete are mainly zeolites (de Gennaro et al. 2000; Jackson 2014). Indeed, phillipsite in the vesicles of pumice clasts in the mortars mainly has intermediate silica compositions that are similar to phillipsite from NYT and Bacoli Tuff (BT), 8.6 ± 0.6 ka (Fedele et al. 2011); these are shown, for example, by most *Portus Neronis* phillipsite compositions (Figs. 3a and 4a; Tables 1 and S1).

Although Roman marine mortar has a mesoscale pumiceous structure that is analogous to the clastic fabric of Campi Flegrei tuff (Figs. 1f–1h), the cementing matrix contains predominantly C-A-S-H binder. In situ dissolution of trachytic glass (Fig. 1f) and alkali feldspar crystal fragments occurred (Fig. 1g), as in the Campi Flegrei tuffs, but the reaction products are not always zeolites. Dissolution of an alkali feldspar crystal fragment in the hardened cementing matrix of the *Portus Neronis* mortar, for example, produced a 100 μm² mold (Fig. 5). Al-tobermorite and strätlingite, a hydrated calcium-aluminum phyllosilicate [$Ca_2Al_2(SiO_2)(OH)_{10}·2.5(H_2O)$], with 12.5 Å (0001) basal spacing, crystallized along the perimeter of the remnant feldspar crystal. Dissolution evidently raised solution ionic concentrations in the mold, and crystalline hydrate precipitation occurred in a leached layer behind the dissolution front (Snellings 2015). Alkali feldspar compositions in the mortars range from potassic (9–12 wt% $K_2O$, 1–2 wt% $Na_2O$ and CaO) to more sodic (5–7 wt% $K_2O$, 3–5 wt% $Na_2O$, and 1–2 wt% CaO).

Vesicles in the perimeter of a pumice clast in the subaerial *Portus Cosanus* mortar contain deeply etched, 15–20 μm Campi Flegrei phillipsite crystals surrounded by C-A-S-H and sub-
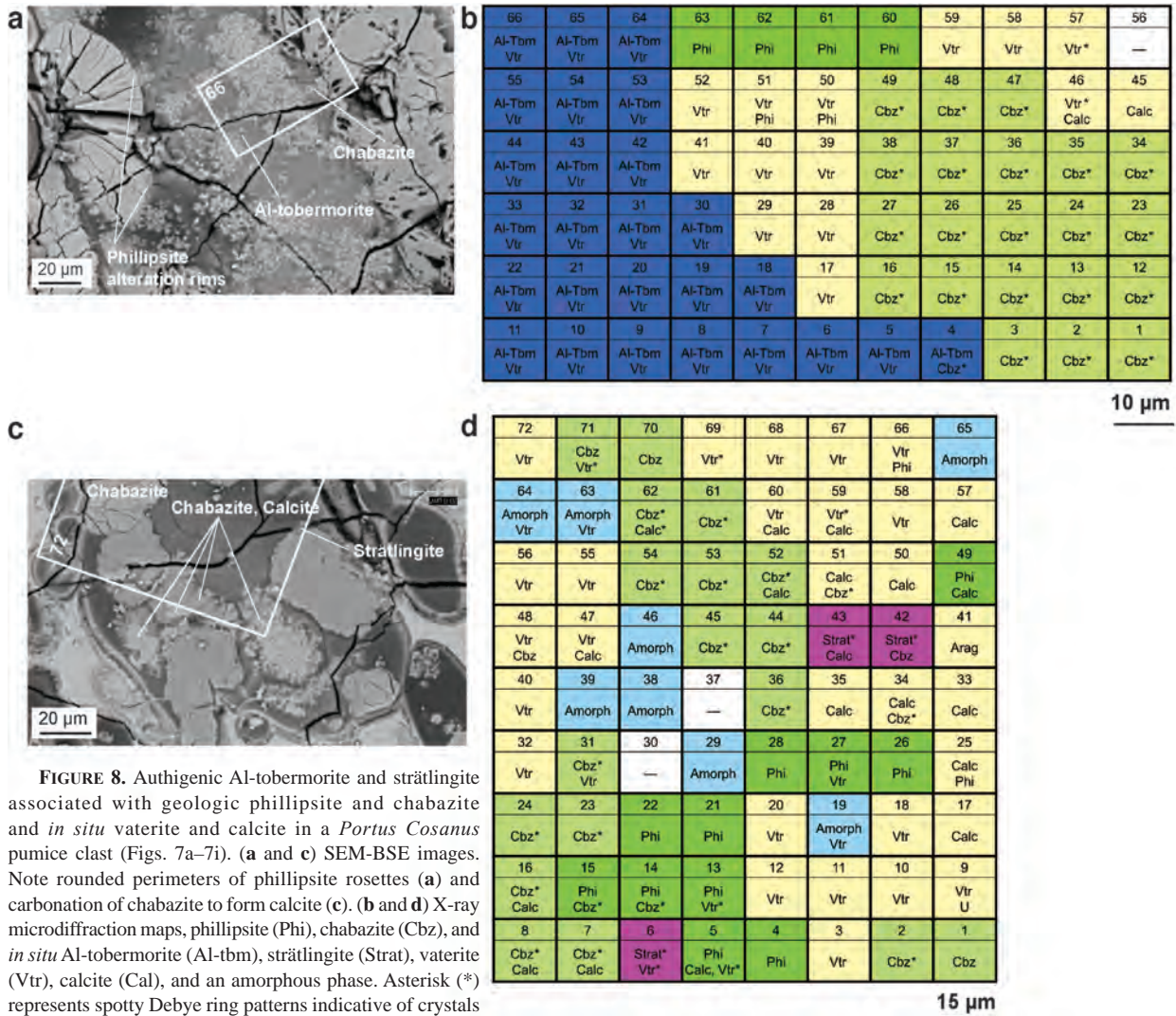
**FIGURE 8.** Authigenic Al-tobermorite and strätlingite associated with geologic phillipsite and chabazite and *in situ* vaterite and calcite in a *Portus Cosanus* pumice clast (Figs. 7a–7i). (**a** and **c**) SEM-BSE images. Note rounded perimeters of phillipsite rosettes (**a**) and carbonation of chabazite to form calcite (**c**). (**b** and **d**) X-ray microdiffraction maps, phillipsite (Phi), chabazite (Cbz), and *in situ* Al-tobermorite (Al-tbm), strätlingite (Strat), vaterite (Vtr), calcite (Cal), and an amorphous phase. Asterisk (*) represents spotty Debye ring patterns indicative of crystals too coarse (>3 µm) to produce regular diffraction rings with the monochromatic X-ray beam. Figure 7i analyses: (**b**) Al-tobermorite (*C*), no. 66, with strong vaterite pattern; (**d**) strätlingite (*D*), no. 06, with weak vaterite pattern.

spherical accumulations of ~5 µm Al-tobermorite (Fig. 1i, locations [1], [2], [3]). These microstructures record deep dissolution of Campi Flegrei phillipsite [1], production of pozzolanic C-A-S-H and Al-tobermorite [2,3], and abrupt termination of pozzolanic reaction before the phillipsite was fully consumed. Experimental mixing of portlandite with phillipsite in Neapolitan Yellow Tuff by Mertens et al. (2009) provides insight into these microstructures. Rapid pozzolanic reaction occurred for a few days until thickening of a reaction rim of hydrates covered the external surfaces of the crystals; the reaction then slowed considerably after 10 days of hydration and proceeded through a diffusion controlled process. The *Portus Cosanus* pumice vesicles evidently record rapid pozzolanic reaction through pH 12–14 pore solutions derived from seawater, calcium hydroxide, and trachytic ash, as Vitruvius described (Appendix Table 1), but sealing of the surfaces of the phillipsite crystals by C-A-S-H and Al-tobermorite hydration products prevented further pozzolanic reaction. Remarkably, the center of this vesicle and adjacent vesicles (Fig. 6a, location [4]) contain masses of <1–2 µm Al-tobermorite crystals, identified through X-ray microdiffraction. These very fine-grained, irregularly shaped agglomerations of Al-tobermorite, which occur as moderate brown, opaque zones in plane-polarized light and cloudy light gray areas in SEM-BSE (Figs. 6b and 6c), seem to have formed subsequently to the sub-spherical accumulations of coarse-grained, pozzolanic Al-tobermorite.

The fine-grained agglomerations of Al-tobermorite in pumice vesicles of the *Portus Cosanus*, *Portus Neronis* (Figs. 6b and 6c) and *Baianus Sinus* mortars are commonly associated with sub-rounded phillipsite aggregations and etched or frayed alkali feldspar crystal fragments. In *Portus Neronis* and *Baianus Sinus* pumice vesicles, Al-tobermorite contains 43.2–47.6 wt% $SiO_2$. These compositions are more siliceous than those of crystals that formed in relict lime clasts in the same mortar specimens,
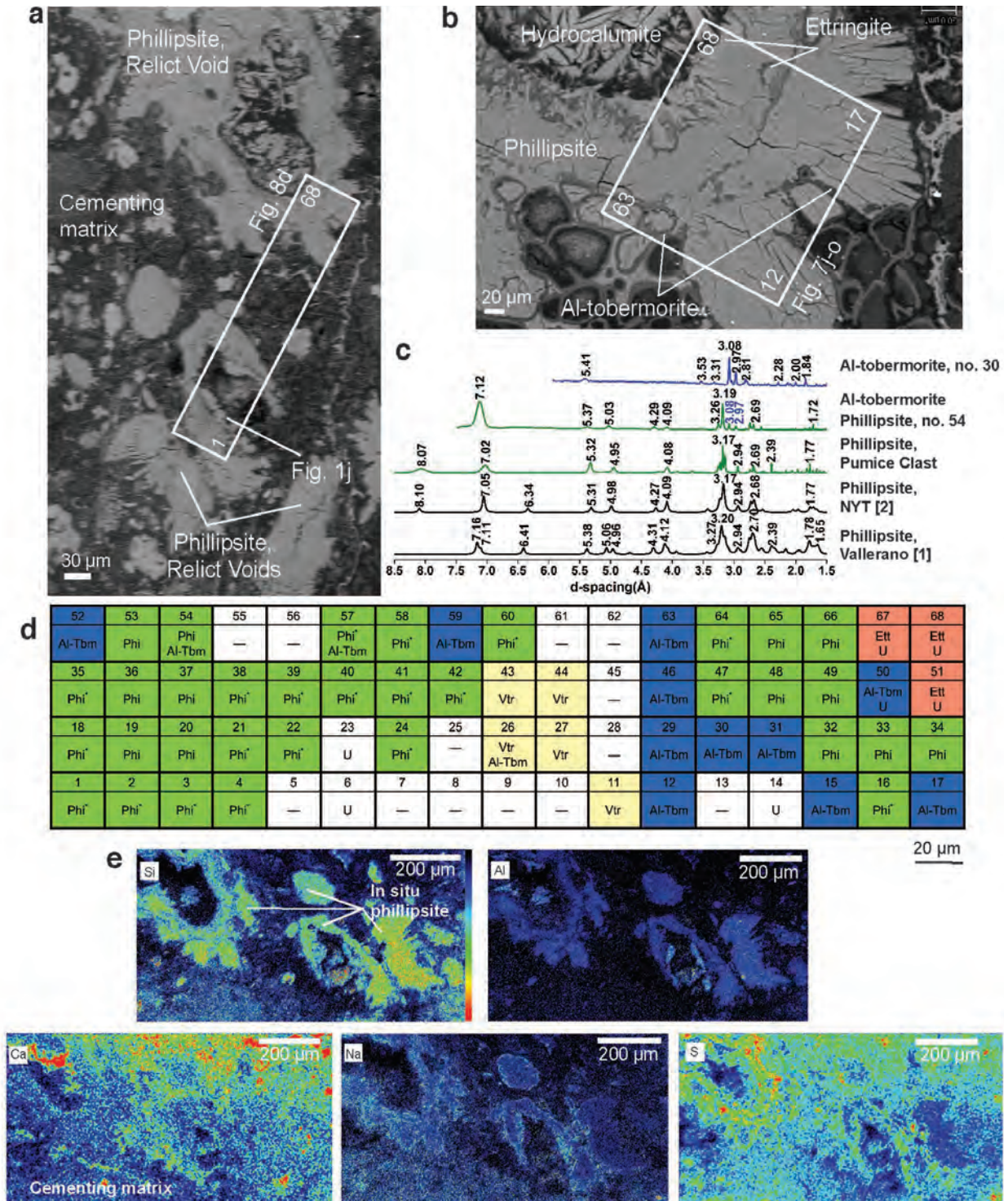
**FIGURE 9.** Authigenic mineral syntheses in relict voids of the cementing matrix, submarine *Baianus Sinus* mortar (Figs. 7j–7o). (**a** and **b**) SEM-BSE images showing relict pores with *in situ* crystalline textures. (**c**) Diffraction patterns for Roman phillipsite and Al-tobermorite in **d** and phillipsite in a *Baianus Sinus* pumice vesicle compared with Campi Flegrei (Gatta et al. 2010) and Alban Hills (Gualtieri 2000) phillipsite. (**d**) X-ray microdiffraction map, showing *in situ* phillipsite (Phi), Al-tobermorite (Al-tbm), ettringite (Ett), vaterite (Vtr), calcite (Cal), unknown (U). Asterisk (*) represents spotty Debye ring patterns indicative of crystals too coarse (>3 μm) to produce regular diffraction rings with the monochromatic X-ray beam. (**e**) SEM-EDS maps, silicon (Si), aluminum (Al), sodium (Na), and sulfur (S) concentrations normalized to 20 mass% (red).
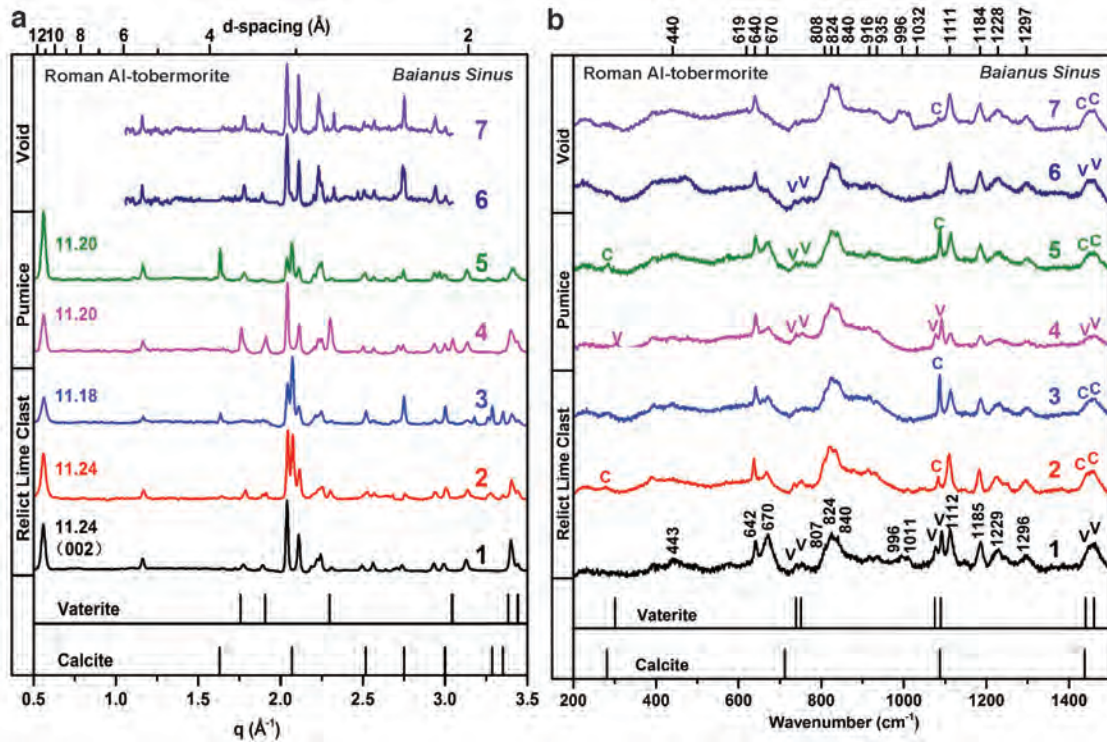
**FIGURE 10.** Al-tobermorite in diverse microstructural environments in *Baianus Sinus* mortar: relict lime clasts, pumice clasts and relict voids. (**a**) X-ray microdiffraction patterns from relict lime clasts, sites (1) LLP_24, (2) SPH3_28, (3) PM_L233; pumice clasts, sites (4) PM_P19, (5) PM_17; relict voids: sites (6) BAIZ_63, (7) BAIZ_15 (see Fig. 9d, locations 63 and 15). (**b**) Raman spectra from the same or nearby crystals in the same microstructures: relict lime clasts: sites (1) LLP_15, (2) SPH3_29, (3) PL_1; pumice clasts, sites (4) PL_4, (5) PL_5; relict voids: sites (6) BAIZ_19, (**7**) BAIZ_17 (see Fig. 9d, near 59). Raman spectra for calcite and vaterite (Behrens et al. 1995; Wehrmeister et al. 2010).
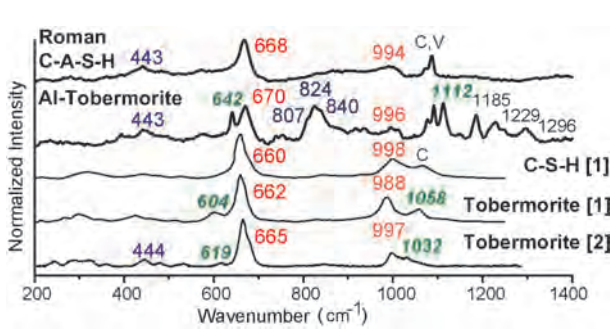


**FIGURE 11.** Raman spectra of *Baianus Sinus* C-A-S-H binder and Al-tobermorite, compared with calcium-silicate-hydrate (C-S-H) binder and ideal tobermorite. Inferred $Q^3$ linkages are shown in italics. Published compositions from [1] Kirkpatrick et al. 1997; [2] http://rruff.info/Tobermorite R060147). Bands at 1074 and 1086 indicate C–O stretching in calcite (C) and vaterite (V).
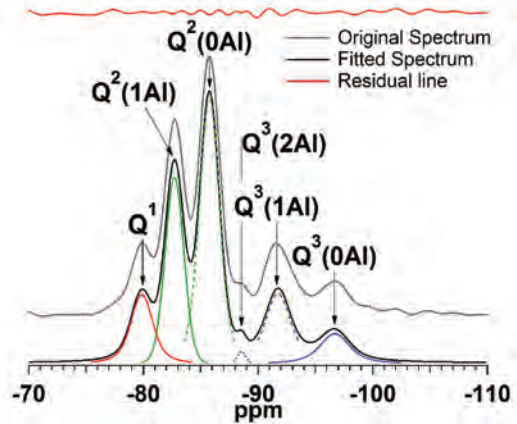


**FIGURE 12.** $^{29}$Si Nuclear magnetic resonance (NMR) of Al-tobermorite in *Baianus Sinus* relict lime clasts (after Jackson et al. 2013b).

and they show a greater range of $Al_2O_3$ and CaO contents (Figs. 3b and 4b, Table 2). Some compositions are nearly identical to Al-tobermorite that crystallized in 15-year-old basaltic tuff of Surtsey volcano, Iceland (Jakobsson and Moore 1986). $Na_2O$ and $K_2O$ at 1.2–3.0 wt% throughout partially balance $Al^{3+}$ substitution for $Si^{4+}$ relative to ideal tobermorite (Mitsuda and Taylor 1978; Komarneni and Roy 1983; Barnes and Scheetz

1991; Taylor 1992). These compositions and the fine-grained habit of the crystals suggest a possible post-pozzolanic origin. They may have precipitated from alkaline fluids in more or less closed chemical systems in vesicles, produced through reaction of feldspar crystals, potassic phillipsite, and trachytic glass, which contains up to 12 wt% $Na_2O+K_2O$ and 2–3 wt% CaO (de Gennaro et al. 2000; Fedele et al. 2011).

**TABLE 1.** Phillipsite compositions measured by EPMA

| | | | *Neapolitan* Yellow Tuff | | Bacoli Tuff (BRI.05.BT) | | *Baianus Sinus* (06-BAI-03) | | *Portus Neronis* (ANZ.02.01) Pumice | | | *Portus Traianus* (PTR.02.02) Void | | Trajan's Markets (GRAULA9) Tufo Lionato | | *Portus Cosanus* (PCO.03.01) Void | |
|---|---|---|---|---|---|---|---|---|---|---|---|---|---|---|---|---|---|
| | | | 1 | 3 | Pumice | Void | Pumice | Void | A | B | C | | | | | 2 | 4 |
| | | | | | | | **wt% oxide** | | | | | | | | | | |
| | LLD[a] | ±2σ[b] | | | | | | | | | | | | | | | |
| $SiO_2$ | 0.04 | 0.45 | 53.1 | 52.0 | 58.6 | 58.8 | 46.7 | 39.5 | 57.3 | 56.1 | 60.2 | 46.0 | 50.1 | 49.5 | 48.8 | 38.9 | 45.3 |
| $TiO_2$ | 0.19 | 0.02 | 0.0 | 0.0 | 0.0 | 0.0 | 0.0 | 0.0 | 0.0 | 0.0 | 0.0 | 0.0 | 0.0 | 0.0 | 0.0 | 0.0 | 0.0 |
| $Al_2O_3$ | 0.04 | 0.24 | 22.3 | 23.7 | 20.2 | 19.3 | 22.8 | 27.6 | 20.9 | 18.6 | 20.2 | 21.4 | 23.4 | 20.3 | 21.2 | 30.7 | 28.4 |
| $Fe_2O_3$ | 0.14 | 0.08 | 0.2 | 0.0 | 0.0 | 0.2 | 0.3 | 0.0 | 0.3 | 0.3 | 0.0 | 0.2 | 0.0 | 0.0 | 0.0 | 0.0 | 0.0 |
| MnO | 0.13 | 0.01 | 0.0 | 0.0 | 0.0 | 0.0 | 0.0 | 0.0 | 0.0 | 0.0 | 0.0 | 0.0 | 0.2 | 0.0 | 0.0 | 0.0 | 0.0 |
| MgO | 0.02 | 0.01 | 0.0 | 0.0 | 0.0 | 0.0 | 0.0 | 0.0 | 0.2 | 0.0 | 0.0 | 0.1 | 0.0 | 0.2 | 0.0 | 0.0 | 0.0 |
| CaO | 0.03 | 0.16 | 7.6 | 8.2 | 1.1 | 0.4 | 2.0 | 10.7 | 1.3 | 0.9 | 1.0 | 4.8 | 4.1 | 4.2 | 5.1 | 8.4 | 7.4 |
| $Na_2O$ | 0.05 | 0.13 | 0.8 | 0.6 | 3.6 | 3.8 | 3.2 | 1.4 | 4.0 | 4.8 | 4.9 | 2.0 | 2.1 | 1.4 | 1.5 | 3.4 | 2.6 |
| $K_2O$ | 0.03 | 0.26 | 7.1 | 7.7 | 9.8 | 10.3 | 5.1 | 2.8 | 7.3 | 8.0 | 8.4 | 7.3 | 8.5 | 8.8 | 8.3 | 10.6 | 8.6 |
| Sum | | | 91.1 | 92.2 | 93.5 | 92.7 | 80.2 | 82.0 | 91.4 | 88.7 | 94.6 | 81.8 | 88.4 | 84.5 | 84.9 | 92.3 | 92.0 |
| $H_2O$[c] | | | 9.0 | 9.0 | 9.2 | 9.1 | 8.0 | 8.0 | 9.1 | 8.8 | 9.4 | 8.0 | 8.6 | 8.3 | 8.3 | 8.5 | 8.8 |
| | | | | | | | **Number of atoms per formula unit based on 16O** | | | | | | | | | | |
| | | ±2σ[d] | | | | | | | | | | | | | | | |
| Si | | 0.4 | 5.3 | 5.2 | 5.7 | 5.8 | 5.2 | 4.4 | 5.6 | 5.7 | 5.8 | 5.2 | 5.2 | 5.4 | 5.3 | 4.1 | 4.6 |
| Ti | | 0.0 | 0.0 | 0.0 | 0.0 | 0.0 | 0.0 | 0.0 | 0.0 | 0.0 | 0.0 | 0.0 | 0.0 | 0.0 | 0.0 | 0.0 | 0.0 |
| Al | | 0.2 | 2.6 | 2.8 | 2.3 | 2.2 | 3.0 | 3.7 | 2.4 | 2.2 | 2.3 | 2.8 | 2.9 | 2.6 | 2.7 | 3.8 | 3.4 |
| $Fe^{3+}$ | | 0.1 | 0.0 | 0.0 | 0.0 | 0.0 | 0.0 | 0.0 | 0.0 | 0.0 | 0.0 | 0.0 | 0.0 | 0.0 | 0.0 | 0.0 | 0.0 |
| Mn | | 0.0 | 0.0 | 0.0 | 0.0 | 0.0 | 0.0 | 0.0 | 0.0 | 0.0 | 0.0 | 0.0 | 0.0 | 0.0 | 0.0 | 0.0 | 0.0 |
| Mg | | 0.0 | 0.0 | 0.0 | 0.0 | 0.0 | 0.0 | 0.0 | 0.0 | 0.0 | 0.0 | 0.0 | 0.0 | 0.0 | 0.0 | 0.0 | 0.0 |
| Ca | | 0.2 | 0.8 | 0.9 | 0.1 | 0.0 | 0.2 | 1.3 | 0.1 | 0.1 | 0.1 | 0.6 | 0.5 | 0.5 | 0.6 | 1.0 | 0.8 |
| Na | | 0.1 | 0.2 | 0.1 | 0.7 | 0.7 | 0.7 | 0.3 | 0.8 | 0.9 | 0.9 | 0.4 | 0.4 | 0.3 | 0.3 | 0.7 | 0.5 |
| K | | 0.3 | 0.9 | 1.0 | 1.2 | 1.3 | 0.7 | 0.4 | 0.9 | 1.0 | 1.0 | 1.1 | 1.1 | 1.2 | 1.1 | 1.4 | 1.1 |
| Sum | | | 9.9 | 10.0 | 10.1 | 10.1 | 10.0 | 10.1 | 10.0 | 10.1 | 10.1 | 10.1 | 10.1 | 10.1 | 10.1 | 11.0 | 10.5 |

[a] 3σ lower limit of detection.
[b] Calculated by stoichiometry.
[c] Average absolute analytical uncertainty on the weight percent oxide.
[d] Average absolute uncertainty on the number of atoms per formula unit, calculated following Giaramita and Day (1990).

**TABLE 2.** Al-tobermorite compositions from *Baianus Sinus* and *Portus Neroni*s measured by EPMA

| | | | *Baianus Sinus* (Bay of Pozzuoli, ROMACONS core BAI.06.03) | | | | | | | *Portus Neronis* (Anzio, ROMACONS core ANZ.02.01) | | | | | | |
|---|---|---|---|---|---|---|---|---|---|---|---|---|---|---|---|---|
| | | | Large Lime Clast | | Pumice Clast | | Lime Clast | | Void | Pumice Clast A1 4 | | | | Pumice Clast A1 6 | | |
| | | | LLP.1 | LLP.2 | PL.2 | PL.4 | PL.7 | PL.8 | Y.17S | | | | | | | |
| | | | | | | | **wt% oxide** | | | | | | | | | |
| | LLD[a] | ±2σ[b] | | | | | | | | | | | | | | |
| $SiO_2$ | 0.06 | 0.39 | 40.1 | 38.4 | 45.5 | 47.6 | 37.9 | 39.9 | 39.0 | 44.2 | 45.5 | 45.7 | 47.5 | 44.8 | 43.2 | 44.6 |
| $Al_2O_3$ | 0.03 | 0.15 | 6.7 | 6.2 | 6.8 | 6.1 | 6.7 | 5.6 | 5.5 | 6.9 | 7.1 | 7.3 | 7.4 | 4.3 | 4.3 | 4.4 |
| $Fe_2O_3$ | 0.19 | 0.07 | 0.0 | 0.0 | 0.0 | 0.0 | 0.2 | 0.0 | 0.0 | 0.0 | 0.3 | 0.3 | 0.3 | 0.0 | 0.0 | 0.0 |
| MgO | 0.02 | 0.04 | 0.1 | 0.2 | 0.0 | 0.0 | 0.3 | 0.3 | 0.0 | 0.1 | 0.2 | 0.1 | 0.2 | 0.0 | 0.0 | 0.0 |
| CaO | 0.05 | 0.49 | 34.5 | 32.7 | 34.1 | 34.5 | 32.5 | 33.4 | 32.1 | 29.0 | 25.8 | 24.2 | 23.5 | 30.2 | 31.2 | 31.7 |
| $Na_2O$ | 0.01 | 0.10 | 0.4 | 1.5 | 0.4 | 0.8 | 1.2 | 2.1 | 2.0 | 0.7 | 0.6 | 1.9 | 0.8 | 1.4 | 2.3 | 1.5 |
| $K_2O$ | 0.03 | 0.09 | 0.6 | 1.0 | 0.8 | 1.0 | 0.7 | 0.6 | 0.9 | 1.1 | 0.9 | 1.6 | 1.4 | 0.4 | 0.7 | 0.5 |
| Sum | | 0.68 | 82.4 | 79.9 | 87.6 | 89.9 | 79.5 | 81.8 | 79.5 | 81.9 | 80.4 | 81.0 | 81.2 | 81.0 | 81.7 | 82.7 |
| $H_2O$[c] | | | 12.2 | 11.7 | 13.2 | 13.5 | 11.7 | 12.0 | 11.7 | 11.8 | 11.8 | 11.9 | 12.1 | 11.7 | 11.6 | 11.8 |
| | | | | | | | **Number of atoms per formula unit based on 18[O,(OH)]** | | | | | | | | | |
| | | ±2σ[d] | | | | | | | | | | | | | | |
| Si | | 0.03 | 4.9 | 4.9 | 5.2 | 5.3 | 4.9 | 5.0 | 5.0 | 5.3 | 5.5 | 5.5 | 5.6 | 5.5 | 5.3 | 5.4 |
| Al | | 0.02 | 1.0 | 0.9 | 0.9 | 0.8 | 1.0 | 0.8 | 0.8 | 1.0 | 1.0 | 1.0 | 1.0 | 0.6 | 0.6 | 0.6 |
| $Fe^{3+}$ | | 0.01 | 0.0 | 0.0 | 0.0 | 0.0 | 0.0 | 0.0 | 0.0 | 0.0 | 0.0 | 0.0 | 0.0 | 0.0 | 0.0 | 0.0 |
| Mg | | 0.01 | 0.0 | 0.0 | 0.0 | 0.0 | 0.0 | 0.1 | 0.0 | 0.0 | 0.0 | 0.0 | 0.0 | 0.0 | 0.0 | 0.0 |
| Ca | | 0.05 | 4.6 | 4.5 | 4.2 | 4.1 | 4.5 | 4.5 | 4.4 | 3.7 | 3.3 | 3.1 | 3.0 | 3.9 | 4.1 | 4.1 |
| Na | | 0.02 | 0.1 | 0.4 | 0.1 | 0.2 | 0.3 | 0.5 | 0.5 | 0.2 | 0.1 | 0.4 | 0.2 | 0.3 | 0.5 | 0.4 |
| K | | 0.01 | 0.1 | 0.2 | 0.1 | 0.1 | 0.1 | 0.1 | 0.1 | 0.2 | 0.1 | 0.2 | 0.2 | 0.1 | 0.1 | 0.1 |
| Sum | | 0.03 | 10.7 | 10.9 | 10.5 | 10.5 | 10.8 | 10.9 | 10.9 | 10.4 | 10.1 | 10.3 | 10.1 | 10.4 | 10.7 | 10.5 |
| | | | | | | | **Cation ratios** | | | | | | | | | |
| Ca/(Al+Si) | | | 0.77 | 0.77 | 0.68 | 0.67 | 0.76 | 0.77 | 0.76 | 0.59 | 0.51 | 0.48 | 0.45 | 0.65 | 0.69 | 0.68 |
| Al/(Al+Si) | | | 0.16 | 0.16 | 0.15 | 0.13 | 0.17 | 0.14 | 0.14 | 0.15 | 0.16 | 0.16 | 0.15 | 0.10 | 0.10 | 0.11 |

[a] 3σ lower limit of detection.
[b] Calculated by stoichiometry.
[c] Average absolute analytical uncertainty on the weight percent oxide
[d] Average absolute uncertainty on the number of atoms per formula unit, calculated following Giaramita and Day (1990).

Although one might suppose that all zeolite in the mortars has a geological origin, phillipsite textures in relict voids of the cementing matrix indicate *in situ* crystallization (Fig. 1h). X-ray microdiffraction analyses of *Baianus Sinus* mortar show, for example, phillipsite clusters that crystallized on Al-tobermorite plates in the cementing matrix (Jackson et al. 2013b). Compared with most Campi Flegrei phillipsite, the phillipsite that formed in relict pores of the marine mortar has lower silica ($SiO_2$, 38–45 wt%), higher alumina ($Al_2O_3$, 28–31 wt%), lower Si/Al (1.3–1.6), and greater calcium (CaO, 7–11 wt%) (Figs. 3a and 4a; Tables 1

**TABLE 3.** Assignments of Raman frequency shifts to silicate and aluminate linkages in *Baianus Sinus* C-A-S-H and Al-tobermorite compared with previous studies of C-S-H and tobermorite

| Previous studies | | | | *Baianus Sinus* mortar | | Inferred Linkage[a,b,c] |
|---|---|---|---|---|---|---|
| Frequency (cm⁻¹) | | | Assignment | Frequency (cm⁻¹) | | |
| C-S-H[a,b] Ca/Si=0.83 | 11Å tobermorite | | | C-A-S-H Ca/(Si+Al) ≈ 0.8[f] | 11Å Al-tobermorite | |
| | a | b | | | | |
| 441–540 | 421 | 444 | $\nu_2(SiO_4)$ Internal deformations | 442–451 | 428–443 | – |
| 600–630 | 604 | 619 | $\nu_4(SiO_4)$ Symmetric bending 600–700 | – | 638–642[g] | SB Q³ (0Al) SB Q³ (1Al) |
| 660–680[a,b,c,d] | 662 | 665 | | 668–671 | 670–671 | SB Q² (0Al) SB Q² (1Al) |
| 850 | – | – | $\nu_1(SiO_4)$ Symmetric stretching 800–1200 | – | 806–809 821–826 837–842 (840–900) | SS Q¹ (0Al) SS Q¹ (1Al) SS Al–O**,i |
| 998–1010[e] | 988 | 997 | | 996 | (913–1012)[h] | SS Q² (0Al) SS Q² (1Al) |
| 1040–1114 | 1058 | 1032 | | (1068 vaterite)[k] | 1110–1113 | SS Q³ (0Al)[j] SS Q³ (1Al) |
| | | | to be determined | | 1228 1250 1297 | |

[a] Kirkpatrick et al. (1997).
[b] Richardson et al. (2010).
[c] http://rruff.info/Tobermorite R060147, Crestmore Quarries, Riverside, California.
[d] Black et al. (2007).
[e] Black (2009), 950–1000 cm⁻¹ band is also attributed to anti-symmetric stretching of Q² silicate linkages.
[f] Jackson et al. (2013).
[g] Frost et al. (1998), FT-Raman analysis of kaolinite, 645 band records SS of (SiO₄) tetrahedral units when the incident laser beam is directed parallel to the *c*-axis of layered crystals.
[h] Weak bands at 913–918, 934–93, 990–1000, 1000–1012.
[i] McMillan and Piriou (1982).
[j] Sharma et al. (1982), 655 band in gehlenite reflects vibrational modes of AlO₄ tetrahedra.
[k] Wehrmeister et al. (2010), vaterite and calcite bands obscure silicate stretching.

and S1). In volcanic deposits and saline lakes, phillipsite crystallizes from pH 8–10 pore fluids (Hay and Iijima 1968; Taylor and Surdam 1981; de Gennaro et al. 2000; Sheppard and Hay 2001); crystal compositions vary with silica activity, salinity, and alkalinity in the fluid phase. Alumina content in phillipsite increases with higher pH pore fluids, but this pH is substantially lower than that of pozzolanic fluids with pH > 12, which are buffered by calcium hydroxide (Lothenbach et al. 2011).

## Maps of post-pozzolanic cementitious microstructures

Synchrotron-based X-ray microdiffraction maps and high-resolution SEM-EDS compositional maps of *Portus Cosanus* and *Baianus Sinus* microstructures provide further insights into diverse pathways for Al-tobermorite crystallization in the Roman mortar fabrics (Fig. 7). In the subaerial *Portus Cosanus* pier intermittently exposed to ingress of seawater and meteoric water, Campi Flegrei phillipsite aggregations that line the vesicle surfaces of a pumice clast have a sub-rounded form with 2–3 μm alteration rims, and/or they are altered to vaterite or calcite; the adjacent chabazite is mainly intact (Figs. 7a–7d). Fine-grained agglomerations of 1–2 μm Al-tobermorite occupy the calcium-enriched internal space of the pumice vesicle, along with vaterite, a metastable calcium carbonate (Figs. 8a and 8b). The Al-tobermorite has large (002) interlayer spacing, 11.41–11.47 Å, indicating substantial $Al^{3+}$ for $Si^{4+}$ (Barnes and Scheetz 1991) [Fig. 7i (analysis *C*)]. A nearby vesicle, however, has Campi Flegrei chabazite and phillipsite that are more strongly altered to vaterite and calcite (Figs. 7e–7h). There, calcium-enriched

areas on the SEM-EDS map correlate with zeolite alteration to vaterite and calcite; no Al-tobermorite is present. Instead, there are occasional strätlingite crystals [Figs. 7i (analysis *D*); 8c, and 8d]. The rounded forms of the phillipsite aggregations (Figs. 7a and 8a), where individual crystal laths have disappeared compared with intact aggregations (Figs. 1h and 9b), suggest possible cation exchange processes. The porous, open, silicate framework of the crystals has a large internal space available for reaction, and repeated cation exchanges occurring along the external surfaces of the laths can decrease the silicate framework, causing the protruding crystals to decompose (Hay 1966). The exchangeable cation reactions would have had a strong influence on alkali concentrations and compositions of solutions within the vesicles, and their crystalline precipitates (Mertens et al. 2009). Overall, the microstructures indicate low-temperature, post-pozzolanic reactions involving zeolite in Campi Flegrei pumice within relatively closed chemical systems at the vesicle scale.

In *Baianus Sinus* breakwater continually submerged in seawater for 2000 yr, the cementing matrix of the mortar contains relict, submillimeter-sized pores filled with 100–200 μm phillipsite fabrics (Figs. 7j–7o). The coarse-grained fabrics formed *in situ*, perhaps associated with alkaline fluids produced by dissolution within a nearby Campi Flegrei vitric tuff clast. SEM-EDS analyses indicate aluminous compositions with 11 wt% potassium and 6 wt% sodium. Hydrocalumite, a platey calcium chloroaluminate $[Ca_2Al(OH)_{6.5}Cl_{0.5}\cdot 3(H_2O)]$, filled the center of the relict voids (Figs. 9a and 9b). Although much of the phillipsite remains intact, areas of higher sodium and sulfur

concentrations coincide with X-ray microdiffraction analyses indicating newly formed cementitious hydrates, mainly ettringite and Al-tobermorite (Figs. 9d and 9e). Ettringite, a hydrous calcium-aluminum-sulfate $[Ca_6Al_2(SO_4)_3(OH)_{12} \cdot 26(H_2O)]$, crystallized in zones with higher sulfur concentrations. Al-tobermorite crystallized in narrow zones with higher calcium and lower silica contents. The acicular crystals protrude from the etched surfaces of the phillipsite fabrics into relict pore space (Fig. 1j). This interfacial relationship is illustrated by X-ray microdiffraction patterns showing both phillipsite and Al-tobermorite at the submicrometer scale (Figs. 9c, 9d, locations 54 and 57). Similar phillipsite and Al-tobermorite mineral assemblages have been described in basaltic tuff at Surtsey volcano, Iceland, at 100 °C 15 years after eruption (Jakobsson and Moore 1986) (Fig. 1e). The *Baianus Sinus* microstructures demonstrate that Al-tobermorite crystallization can occur at ambient seawater temperatures, 14–26 °C (Damiani et al. 1987), in a highly potassic and sodic system produced through alteration of phillipsite, which itself precipitated in the mortar fabric. The complex mineral textures indicate cycling of low-temperature, post-pozzolanic reactions in pores of the cementing matrix as a response to evolving fluid interactions over time.

**Raman spectroscopy**

Raman spectroscopic analyses referenced to previous $^{29}$Si and $^{27}$Al nuclear magnetic resonance (NMR) studies provide insights into the roles of $Al^{3+}$, $Na^+$, and $K^+$ in *Baianus Sinus* Al-tobermorite from diverse microstructural environments, as compared with ideal tobermorite $[Ca_5Si_6O_{17} \cdot 5H_2O$ (Biagioni et al. 2015)], *Baianus Sinus* C-A-S-H, and calcium-silicate-hydrate C-S-H binder (Figs. 10–12). X-ray microdiffraction analyses of Al-tobermorite in relict lime clasts, pumice clasts, and relict voids show relatively uniform patterns, with 11.20–11.24 Å interlayer spacing, modified mainly by the relative intensity of vaterite and calcite reflections (Fig. 10a). Raman spectra of the same or adjacent crystals mainly show a 670–671 cm$^{-1}$ band corresponding to symmetrical bending (SB) of $Q^2$(0Al) linkages of middle chain silicon tetrahedra (Kirkpatrick et al. 1997; Richardson et al. 2010) (Fig. 10b). A sharp 1111–1112 band indicates symmetrical stretching (SS) of bridging $Q^3$(1Al) linkages (Richardson et al. 2010). These linkages are shown in NMR study of *Baianus Sinus* Al-tobermorite in relict lime clasts (Jackson et al. 2013a, 2013b) (Fig. 12); the ~1040–1080 band associated with SS $Q^3$(0Al) is, however, obscured by carbonate bands. A 638–642 band corresponds to SB of $Q^3$(0Al) (Kirkpatrick et al. 1997) and $Q^3$(1Al). The SB and SS $Q^3$ bands indicate linkages across the (002) interlayer, which contains channels for water molecules and exchangeable alkali cations (Tsuji and Komarneni 1989; Yamazaki and Toraya 2001). A ~840–900 shoulder indicates SS of $Q^1$(0Al) sites (McMillan and Piriou 1982). A prominent 800–840 maximum not detected in ideal tobermorite (Fig. 11) may indicate both Al–O stretching and $Q^1$ motions of silica and aluminum against tetrahedral oxygen (McMillan and Piriou 1982).

Roman Al-tobermorite spectra shows substantial variation from the spectra of ideal tobermorite (Fig. 11, Tobermorite [1],[2]). In ideal tobermorite, SS $Q^2$ linkages assigned to 950–1010 cm$^{-1}$ (Richardson et al. 2010) occur as a broad band centered

at 998. There is little band definition, however, in Roman Al-tobermorite in this region, with the exception of analysis 7 (Fig. 10b), which corresponds to an X-ray microdiffraction site where Al-tobermorite crystallized in the interfacial zone of *in situ* phillipsite aggregations (Fig. 9d, location 15). In crystals and glasses of silica-alumina systems, highly condensed aluminate tetrahedra may lead to geometric distortion, loss of vibrational coherence and observed band structure (McMillan and Piriou 1982; McMillan et al. 1982). Substantial $Q^2$(1Al) relative to $Q^2$(0Al) occurs in $^{29}$Si and $^{27}$Al NMR study of Roman Al-tobermorite in relict lime clasts (Fig. 12), as well as in cross-linked Al-tobermorite synthesized through pozzolanic interaction of NaOH-activated trachytic volcanic rock with calcium hydroxide (Youssef et al. 2010). This suggests that abundant $Al^{3+}$ substitution for $Si^{4+}$ may dampen the expression of the SS $Q^2$(0Al) linkages, causing loss of the SS $Q^2$ band, but quantification of these relationships is beyond the scope of this article. SS $Q^1$ in ideal tobermorite appears as a broad, low-intensity band centered at 850. Roman Al-tobermorite, instead, has an asymmetric maximum at 807–840 that leads to a weak shoulder at ~840–900. The shoulder may indicate SS $Q^1$(0Al), but the maxima composed of 806–809, 821–826, and 837–842 bands may indicate a component of Al–O stretching (McMillan and Piriou 1982; McMillan et al. 1982), which occurs at 796–804 and 841 in certain calcium-alumina-silicate crystals (Sharma et al. 1982). NMR studies of sodic and potassic C-A-S-H [C-(N,K-)A-S-H] show increased $Q^1$ intensity with Na and K content; binding of silica to $Na^+$ and $K^+$ rather than $Ca^{2+}$ in the interlayer and the CaO surface leads to more silica dimers, shorter silicate chain lengths, and increased $Q^1$ (Myers et al. 2015b; L'Hôpital et al. 2016). A +3 ppm shift of $Q^3$(1Al) in $^{29}$NMR study of Roman Al-tobermorite (Fig. 11) also suggests a greater proportion of monovalent cations relative to $Ca^{2+}$ (Myers et al. 2015b). The Al-tobermorite 800–840 maxima may thus correspond to complex $Q^1$(0Al) and $Q^1$(1Al) sites and, perhaps, coupled $[Al^{3+}+Na^+]$ substitution, similar to laboratory syntheses in which tetrahedrally coordinated $Al^{3+}$ substitutes for $Si^{4+}$ and $Cs^+$ selectively exchanges for $Na^+$ in the cross-linked (002) interlayer (e.g., Tsuji and Komarneni 1989; Coleman et al. 2014).

SB $Q^2$ in ideal tobermorite and C-S-H is assigned to 650–680 cm$^{-1}$ (Kirkpatrick et al. 1997, Richardson et al. 2010; Black 2009). The absence of the 670–671 band in Al-tobermorite associated with phillipsite alteration in relict voids where qualitative EDS analyses indicate high alumina (Figs. 7j–7n and 9e), suggests that condensed aluminate tetrahedra could contribute to loss of the silicate band structure (McMillan and Piriou 1982; McMillan et al. 1982), as for SS $Q^2$. SB of $Q^3$ linkages in ideal tobermorite is assigned to 620 (Kirkpatrick et al. 1997), apparently based on a metasilicate band group at 1050, 980, and 650 and vibrational similarities with a $SiO_2$–$CaAl_2O_4$ glass series (McMillan et al. 1982). The 638–642 band in Roman Al-tobermorite could therefore correspond to SB $Q^3$(0Al) and $Q^3$(1Al), associated with SS Q3 vibrations at 1111 and obscured at 1080. $^{27}$Al NMR of crystals from relict lime clasts records these tetrahedral $Q^3$(1Al) linkages through a peak at 57.70 ppm (Jackson et al. 2013a, 2013b). Distortions of $AlO_4$ tetrahedral bond lengths and complexities in Al–O coordination in Roman Al-tobermorite in relict lime clasts are indicated by NEXAFS

spectra, where a tetrahedral 1566.7 eV absorption edge broadens to an octahedral 1571.0 eV absorption edge. These complexities may also be recorded by $^{27}$Al NMR, which has a weak octahedrally coordinated $Al_2O_6$ component at 10.88 ppm (Jackson et al. 2013a, 2013b). Components of both Al–O stretching and complex motions of silica and aluminum against tetrahedral oxygen may therefore occur at the Raman 443 and the 800–840 maxima (McMillan and Piriou 1982; McMillan et al. 1982). It is not clear how these spectra might record possible octahedrally coordinated $Al^{3+}$ substitution for $Ca^{2+}$ within the interlayer of the crystals (Abdolhosseini Qomi et al. 2012).

*Baianus Sinus* C-A-S-H shows uniform Raman spectra over a diverse range of cementitious microstructures (Fig. 11). A broad band centered at 668 cm$^{-1}$ corresponds to symmetrical bending (SB) of Q$^2$(0Al), and could also include SB of Q$^2$(1Al), given the tetrahedral aluminum 1566.7 eV absorption edge recorded by NEXAFS spectra of C-A-S-H in relict lime clasts (Jackson et al. 2013a). SS Q$^2$ linkages occur as a broad band centered at 994. Spectra indicating SS Q$^3$(0Al) and a cross-linked structure at ~1040–1080 band are, however, obscured by carbonate bands.

## Authigenic mineral cycling

Alteration of tephra deposits occurs when interstitial water becomes modified through hydrolysis or dissolution of volcanic ash components. These reactions release hydroxyl ions, and the solution becomes more alkaline and enriched in Na, K, Ca, and Si along its flow path. Zeolites crystallize when the cation to hydrogen ion ratio and other ionic activities are relatively high (Sheppard and Hay 2001). Early-formed zeolites commonly alter to other zeolites; phillipsite, for example, commonly alters to analcime, and analcime can be replaced by laumontite, K-feldspar, or albite (Hay and Sheppard 2001). Authigenic textures thus record dynamic physico-chemical environments and phase-stability relationships over time in open-to-closed hydrologic systems.

In Campi Flegrei deposits, post-eruptive hydrolysis and dissolution of trachytic glass in the presence of condensed water vapor generated alkaline fluids from which zeolites originated (Figs. 1b–1d) (de Gennaro et al. 1999). Airfall deposits from highly expanded ash clouds with limited water-magma interaction are less zeolitized than hydromagmatic deposits that retain pore water and water vapor, grow zeolite mineral cements, and lithify to form tuff. By first century BCE, Roman engineers had identified the unconsolidated pumiceous ash deposits, or *pozzolana*, as the optimum aggregate (*pulvis*) for maritime concrete harbor mortars; they used lithified zeolitized tuff deposits as coarse aggregate (*caementa*) in the concrete (Stanislao et al. 2011; Jackson 2014). When they installed the pumiceous ash and lime mortar mixture hydrated with seawater in subaerial and submarine structures, they created a highly alkaline but relatively short-lived pozzolanic system buffered by calcium hydroxide, which produced C-A-S-H and Al-tobermorite at ≤95 °C in lime clasts (Jackson et al. 2013a). Pozzolanic reaction of Campi Flegrei phillipsite in the perimetral vesicles of pumice clasts in response to infiltration of the high pH fluids also produced C-A-S-H and Al-tobermorite (Figs. 1i and 6a). Rates of reaction may have been on the order of days or weeks, based on experimental mixing of portlandite and distilled water with phillipsite at 40 °C with

phillipsite from Neapolitan Yellow Tuff (Mertens et al. 2009). The mortar reaction became diffusion controlled and eventually terminated when C-A-S-H and Al-tobermorite accumulations enveloped the phillipsite aggregations. Consumption of portlandite in the large Roman harbor structures was likely complete within 5–10 yr, based on an experimental concrete reproduction (Oleson et al. 2006; Jackson 2014), an adiabatic model of heat evolved in the *Baianus Sinus* breakwater (Jackson et al. 2013a), and observations of pozzolanic systems with pyroclastic rock pozzolans (Massazza 1985, 2004). This is in contrast to Portland cement concretes that maintain very high pH and alkalinity over the long term, since portlandite saturation and free portlandite in pore fluids persist for extended periods of time.

In the post-pozzolanic hydrologic system of the massive Roman concrete structures open to seawater and/or meteoric water ingress, residual components of the pumiceous ash—feldspar crystal fragments, authigenic phillipsite, and trachytic glass—reacted with interstitial fluids at low temperature to produced alkaline pore solutions in diverse components of the mortar fabric. Al-tobermorite (and strätlingite) crystallized in the leached perimeters of Campi Flegrei feldspar fragments (Figs. 1g and 5) and in pumice vesicles in response to dissolution or decomposition of Campi Flegrei phillipsite (and chabazite) (Figs. 6, 7a–7i, and 8). *In situ* crystallization of phillipsite occurred in relict pores throughout the cementing matrix (Figs. 1h, 7j–7o, and 9), apparently at ambient seawater temperatures, 14–28 °C, after exothermic heat evolution through pozzolanic reaction was complete. Al-tobermorite then crystallized in the interfacial zones of these phillipsite fabrics. These crystals resemble those that crystallized from dissolving phillipsite in 15-year-old palagonitized basaltic tuff of Surtsey volcano, Iceland, but at 100 °C (Figs. 1e and 1j).

Al-tobermorite is considered to have a hydrothermal origin in geologic occurrences (Claringbull and Hey 1952; Mitsuda and Taylor 1978; Livingstone 1988; Henmi and Kusachi 1992; Hoffman and Armbruster 1997; Aguirre et al. 1998) and has been previously produced in laboratory syntheses always at ≥80 °C (e.g., Komarneni and Roy 1983). Alkali-activated pozzolanic production of zeolite and Al-tobermorite has been produced in autoclaved aerated concrete, heated at 110–200 °C in 12 h to 7 days (Grutzeck et al. 2004), and through NaOH-activated trachytic rock aggregate mixed with calcium hydroxide and heated at 150–175 °C for 24 h (Youssef et al. 2010). Relatively low-temperature crystallization of phillipsite and Al-tobermorite has occurred, however, in the pores of Portland cement paste in contact with a claystone interface at 70 °C one year after installation (Lalan et al. 2016). Furthermore, Al-tobermorite has been identified throughout a 181 m core drilled through Surtsey in 1979, at temperatures from 25 °C in surficial deposits to 140 °C in hydrothermally altered tuff (Jakobsson and Moore 1986) (see Fig. 1e). The distinguishing feature of the Roman marine mortar system is to record low-temperature processes of authigenic mineral cycling, which involve the reaction of volcanic ash components; production of alkaline fluids in microenvironments; precipitation of new minerals, principally phillipsite in these microstructures; and evolving pore solution chemistries that produce Al-tobermorite crystallization in subaerial and submarine structures.

Systems that begin as relatively simple states and evolve to states of increasing complexity are a recurrent characteristic of mineral evolution and Earth processes, as well as emerging technologies (Hazen et al. 2008). Vitruvius described the relatively simple mixture of volcanic ash (*pulvis*), lime (*calx*), and tuff aggregate (*tofus*) that cohered pozzolanically in seawater. Pliny the Elder and Seneca called upon geologic analogs to explain concrete resilience after 100–150 yr of service life. Advanced analytical techniques now show the complexity of Roman marine concrete technologies, whose initial protocols for developing an effective pozzolanic cementitious system evolved through authigenic mineral cycling to produce cementitious systems with the chemical range and longevity of water-rock interactions in pyroclastic rocks of Earth's upper crust. Roman builders evidently had these objectives in mind when designing the maritime concrete structures (Brandon et al. 2014).

The cementing fabrics of Roman concrete breakwaters and piers constructed with volcanic ash mortars provide a well-constrained template for developing cementitious technologies through low-temperature rock-fluid interactions, cation-exchange, and carbonation reactions that occur long after an initial phase of reaction with lime that defines the activity of natural pozzolans (Massazza 2004). Some aspects of the Roman post-pozzolanic system have been reproduced by geopolymer-type cementitious systems, where alkali mediated dissolution and precipitation reactions involving little or no calcium occur in aqueous reaction substrates (Provis and Bernal 2014). These systems do not, however, produce on-going, beneficial precipitation of cementitious hydrates through evolving alteration of reactive aggregate(s). Coupled dissolution and precipitation processes produced through the reactivity of synthetic calcium (alumino)silicate glasses, basaltic glasses, and borosilicate glasses with aqueous solutions at varying pH (Snellings 2015; Jantzen et al. 2017) have a great deal of relevance for gaining further understanding of multiple pathways to low-temperature Al-tobermorite crystallization. This especially concerns variable solution chemistries produced in microenvironments associated with authigenic dissolution of the alkaline components of pozzolanic volcanic ash—alkali feldspar, trachytic glass, and relict zeolite textures. Carbonation of zeolite in the pumice clasts of the subaerial mortar also apparently released alkaline earth elements associated with low-temperature crystallization of Al-tobermorite. The platy and acicular Al-tobermorite crystals may increase ductility and resistance to fracture (Jackson et al. 2014), possibly leading to the increasing mechanical resilience of the concrete that Pliny observed […and stronger every day (*fortiorem cotidie*) (Appendix Table 1)].

## IMPLICATIONS

That *in situ* production of alkaline pore fluids derived from low-temperature interactions of seawater-derived fluids with components of trachytic Campi Flegrei pumiceous ash drives zeolite and Al-tobermorite crystallization in Roman marine concrete is a surprising discovery, since (1) laboratory Al-tobermorite syntheses have not been produced at ambient temperatures, and (2) release of alkali cations from rock aggregate in Portland cement concrete generally produces expansive alkali-silica gels that degrade structural concretes worldwide. By contrast, the alkaline fluids in Roman subaerial and submarine concrete piers and breakwaters produce precipitation of phillipsite and Al-tobermorite mineral cements that refine pore space, enhance bonding in pumice clasts and sequester alkali cations, principally sodium and potassium.

Roman marine concretes can provide guidelines for the optimal selection of natural volcanic pozzolans that have the potential to produce of regenerative cementitious resilience through long-term crystallization of zeolite, Al-tobermorite, and strätlingite mineral cements. The cross-linked structure and $Al^{3+}$ bonding environments of the Roman Al-tobermorite crystals, recorded by Raman spectra through a range of cementitious microstructures and crystallization pathways, provide clues to creating new pathways for cation-change in high-performance concretes. Furthermore, the chemical and mechanical resilience of the marine concrete provides keys to understanding dynamic mineral cements in young, oceanic pyroclastic deposits, as at Surtsey (Jakobsson and Moore 1986), the seismic response of a volcanic edifice, as in deep Campi Flegrei deposits (Vanorio and Kanitpanyacharoen 2015), and carbon mineralization reactions, as occur in porous basaltic storage reservoirs for anthropogenic $CO_2$ (Matter et al. 2016). Roman prototypes for brine-based concretes could conserve freshwater resources, generate multiple low temperature pathways to pozzolanic and post-pozzolanic Al-tobermorite sorbents with coupled $Al^{3+}$ and exchangeable alkali cation sites, and extend applications of natural volcanic pozzolans to environmentally friendly, alkali-activated structural concretes and cementitious barriers for waste encapsulations.

## REFERENCES CITED

Abdolhosseini Qomi, M.J., Ulm, F.-J., and Pellenq, R.J.-M. (2012) Evidence on the dual nature of aluminum in the calcium-silicate-hydrates based on atomistic simulations. Journal of the American Ceramic Society, 95, 1128–1137.

Aguirre, L., Dominguez-Bell, S., Morata, D., and Winke, O. (1998) An occurrence of tobermorite in Tertiary basalts from Patagonia, Chile. Canadian Mineralogist, 36, 1149–1155.

ASTM (2015) Standard specification for coal fly ash and raw or natural pozzolan for use in concrete (C618-15). ASTM International, West Conshohocken, Pennsylvania, www.astm.org.

Barnes, M.W., and Scheetz, B.E. (1991) The chemistry of Al-tobermorite and its coexisting phases at 175 °C. In B.E. Scheetz, A.G. Landers, I. Oder, and H. Jennings, Eds., Specialty Cements with Advanced Properties, 179, 243–271. Material Research Society Symposium Proceedings, Warrendale, Pennsylvania.

Behrens, G., Kuhn, L.T., Ubic, R., and Heuer, A.H. (1995) Raman spectra of vateritic calcium carbonate. Spectroscopy Letters, 28, 983–995.

Biagioni, C., Merlino, S., and Bonaccorsi, E. (2015) The tobermorite supergroup: A new nomenclature. Mineralogical Magazine, 79, 485–495.

Black, L. (2009) Raman spectroscopy of cementitious materials. Spectroscopic Properties Inorganic Organometric Compounds, 40, 72–127.

Black, L., Breen, C., Yarwood, J., Garbev, K., Stemmerman, P., and Gasharova, B. (2007) Structural features of C–S–H(I) and its carbonation in air—A Raman spectroscopic study. Part II: Carbonated phases. Journal of the American Ceramic Society, 90, 908–917.

Brandon, C., Hohlfelder, R.L., Jackson, M.D., and Oleson, J.P. (2014) Building for Eternity: The History and Technology of Roman Concrete Engineering in the Sea.

Oxbow Books, Oxford, 327 p.

Brune, P.F., Ingraffea, A.R., Jackson, M.D., and Perucchio, R. (2013) The fracture toughness of an Imperial Roman mortar. Engineering Fracture Mechanics, 102, 65–76.

Cai, G., Noguchi, T., Degée, H., Zhao, J., and Kitagaki, R. (2016) Volcano-related materials in concretes: a comprehensive review. Environmental Science and Pollution Research, 23, 7220–7243.

Celik, K., Jackson, M.D., Mancio, M., Meral, C., Emwas, A.M., Mehta, P.K., and Monteiro, P.J.M. (2014) High-volume natural volcanic pozzolan and limestone powder as partial replacements for Portland cement in self-compacting and sustainable concrete. Cement and Concrete Composites, 45, 136–147.

Claringbull, G.F., and Hey, M. (1952) A re-examination of tobermorite. Mineralogical Magazine, 29, 960–962.

Coleman, N.J., Li, Q., and Raza, A. (2014) Synthesis, structure and performance of calcium silicate ion exchangers from recycled container glass. Physicochemical Problems in Mineral Processing, 50, 5–16.

Damiani, V. Baudo, R. De Rosa, S., De Simone, R., Ferretti, O., Izzo, G., and Serena, F. (1987) A case study: Bay of Pozzuoli (Gulf of Naples, Italy). Hydrobiologia, 149, 201–211.

de Gennaro, M., Incoronato, A., Mastrolorenzo, G., Adabbo, M., and Spina, G. (1999) Depositional mechanisms and alteration processes in different types of pyroclastic deposits from Campi Flegrei volcanic field (Southern Italy). Journal of Volcanological and Geothermal Research, 91, 303–320.

de Gennaro, M., Cappelletti, P., Langella, A., Perrotta, A., and Scarpati, C. (2000) Genesis of zeolites in the Neapolitan Yellow Tuff: Geological, volcanological and mineralogical evidence. Contributions to Mineralogy and Petrology, 139, 17–35.

Deer, W.A., Howie, R.A., Wise, W.S., and Zussman, J. (2004) Rock-forming minerals. Vol. 4B, Framework silicates: silica minerals, feldspathoids and the zeolites. Geological Society of London, U.K.

Fedele, L., Insinga, D.D., Calvert, A.T., Morra, V., Perrotta, A., and Scarpati, C. (2011) $^{40}Ar/^{39}Ar$ dating of tuff vents in the Campi Flegrei caldera, southern Italy. Bulletin of Volcanology 73, 1323–1336.

Frost, R.L., Tran, T.H., Rintoul, L., and Kristol, J. (1998) Raman microscopy of dickite, kaolinite, and their intercalates. Analyst, 123, 611–616.

Gatta, G.D., Cappelletti, P., and Langella, A. (2010) Crystal chemistry of phillipsites from the Neapolitan Yellow Tuff. European Journal of Mineralogy, 22, 779–786.

Gaucher, E.C., and Blanc, P. (2006) Cement/clay interactions—A review: Experiments, natural analogues, and modeling. Waste Management, 26, 776–788.

Giaramita, M.J., and Day, H.W. (1990) Error propagation in calculations of structural formulas. American Mineralogist, 75, 170–182.

Goñl, S., Lorenzo, M.P., Guerrero, A., and Hernández, M.S. (2005) Calcium hydroxide saturation factors in the pore solution of hydrated portland cement fly ash paste. Journal of the American Ceramic Society, 79, 1041–1046.

Gotti, E., Oleson, J.P., Bottalico, L., Brandon, C., Cucitore, R., and Hohlfelder, R.L. (2008) A comparison of the chemical and engineering characteristics of ancient Roman hydraulic concrete with a modern reproduction of Vitruvian hydraulic concrete. Archaeometry, 50, 576–590.

Grutzeck, M., Kwan, S., and DiCola, M. (2004) Zeolite formation in alkali-activated cementitious systems. Cement and Concrete Research, 34, 949–955.

Gualtieri, A.F. (2000) Accuracy of XRPD QPA using the combined Rietveld-RIR method. Journal of Applied Crystallography, 33, 267–278.

Hay, R.L. (1966) Zeolite and zeolite reactions in sedimentary rocks. Geological Society of America Special Paper 85.

Hay, R.L., and Iijima, A. (1968) Nature and origin of palagonite tuffs of the Honolulu group on Oahu, Hawaii. Geological Society of America Memoir, 116, 331–376.

Hay, R.L., and Sheppard, R.A. (2001) Occurrence of zeolites in sedimentary rocks: an overview. Reviews in Mineralogy and Geochemistry, 45, 217–234.

Hazen, R.M., Papineau, D., Bleeker, W., Downs, R.T., Ferry, J.M., McCoy, T.J., Sverjensky, D.A., and Yang, H. (2008) Mineral evolution. American Mineralogist, 93, 1693–1720.

Henmi, C., and Kusachi, I. (1992) Clinotobermorite, $Ca_5Si_6(O, OH)_{18}5H_2O$, a new mineral from Fuka, Okayama Prefecture, Japan. Mineralogical Magazine, 56, 353–358.

Hoffman, C., and Armbruster, T. (1997) Clinotobermorite, $Ca_5[Si_3O_8(OH)]_{24} H_2O$, a natural C-S-H(I) type cement mineral: Determination of the substructure. Zeitschrift für Kristallographie, 212, 864-873.

Jackson, M.D. (2014) Seawater concretes and their material characteristics. In J.P. Oleson, Ed., Building for Eternity: the History and Technology of Roman Concrete Engineering in the Sea, p. 141–187, Oxbow Books, Oxford.

Jackson, M.D., and Kosso, K. (2013) Scientia in republican era stone and concrete masonry. In J.R. Evans, Ed., A Companion to the Archaeology of the Roman Republic, 1st ed., p. 268–284, Blackwell, New York.

Jackson, M.D., Vola, G., Všiansky, D., Oleson, J.P., Scheetz, B., Brandon, C., and Hohlfelder, R.L. (2012) Cement microstructures and durability in ancient Roman seawater concretes. In J. Válek, C. Groot, and J. Hughes, Eds., Historic Mortars, Characterisation, Assessment and Repair, p. 49–76, Springer, Berlin.

Jackson, M.D., Chae, S.R., Mulcahy, S.R., Meral, C., Taylor, R., Li, P., Emwas, A.H., Moon, J., Yoon, S., Vola, G., and others. (2013a) Unlocking the secrets of Al-tobermorite in Roman seawater concrete. American Mineralogist, 98, 1669–1687.

Jackson, M.D., Moon, J., Gotti, E., Taylor, R., Chae, S.R., Kunz, M., Emwas, A-H., Meral, C., Guttman, P., Levitz, P., and others. (2013b) Material and elastic properties of Al-tobermorite in ancient Roman seawater concrete. Journal of the American Ceramic Society, 96, 2598–2606.

Jackson, M.D., Landis, E.N., Brune, P.B., Vitti, M., Chen, H., Li, Q., Kunz, M., Wenk, H.-R., Monteiro, P.J.M., and Ingraffea, A.R. (2014) Mechanical resilience and cementitious processes in Imperial Roman architectural mortar. Proceedings of the National Academy of Sciences, 111, 18485–18489.

Jakobsson, S., and Moore, J.G. (1986) Hydrothermal minerals and alteration rates at Surtsey volcano, Iceland. Geological Society of America Bulletin, 97, 648–659.

Jantzen, C.M., Crawford, C.L., Trivelpiece, C., Pareizs, J.M., and Picket, J.B. (2017) Accelerated Leach Testing of GLASS (ALTGLASS): II. Mineralization of Hydrogels by Leachate Strong Bases. International Journal of Applied Glass Science, 8, 84–96 (SRNL-STI-2014-00381).

Komarneni, S., and Roy, D. (1983) Tobermorites: A new family of cation exchangers. Science, 221, 647–648.

Komarneni, S., Breval, E., Miyake, M., and Roy, R. (1987) Cation exchange properties of (Al+Na)-substitutes synthetic tobermorites. Clays and Clay Minerals, 35, 385–390.

Kirkpatrick, R.J., Yarger, J.L., McMillan, P.F., Yu, P., and Cong, X. (1997) Raman spectroscopy of C-S-H, tobermorite, and jennite. Advances in Cement Based Materials, 5, 93–99.

Lalan, P., Dauzères, A., DeWindt, L., Bartier, D., Sammaljärvi, J., Barnichon, J.-D., Techer, I., and Detilleux, V. (2016) Impact of a 70 °C temperature on an ordinary Portland cement paste/claystone interface: An in situ experiment. Cement and Concrete Research, 83, 164–178.

L'Hôpital, E.L., Lothenbach, B., Scrivener, K., and Kulik, D.A. (2016) Alkali uptake in calcium alumina silicate hydrate (C-A-S-H). Cement and Concrete Research, 85, 122–136.

Livingstone, A. (1988) Reyerite, tobermorite, calcian analcime and bytownite from amygdules in Skye basalt. Mineralogical Magazine, 52, 711–713.

Lothenbach, B., Scrivener, K., and Hooton, R.D. (2011) Supplementary cementitious materials. Cement and Concrete Research, 41, 217–229.

Marra, F., Jackson, M.D., Deocampo, D., and Ventura, G. (2009) Large mafic eruptions at Alban Hills Volcanic District (Central Italy). Journal of Volcanic and Geothermal Research, 179, 217–232.

Massazza, F. (1985) Concrete resistance to seawater and marine environment. Il Cemento, 82, 26–85.

——— (2004) Pozzolana and pozzolanic cements. In P.C. Hewlett, Ed., Lea's Chemistry of Cement and Concrete, 4th ed., p. 471–602, Elsevier, Oxford.

Matter, J.M., Stute, M., Snæbjörnsdottir, S.Ó., Oelkers, E.H., Gislason, S.R., Aradottir, E.S., Sigfusson, B., Gunnarsson, I., Sigurdardottir, H., Gunnlaugsson, E., and others. (2016) Rapid carbon mineralization for permanent disposal of anthropogenic carbon dioxide emissions. Science, 352, 1312–1314.

McMillan, P., and Piriou, B. (1982) The structures and vibrational spectra of crystals and glasses in the silica-alumina system. Journal of Non-Crystalline Solids, 53, 279–298.

McMillan, P., Piriou, B., and Navrotsky, A. (1982) A Raman spectroscopic study of glasses along the joins silica-calcium aluminate, silica-sodium aluminate, and silica-potassium aluminate. Geochimica and Cosmochimica Acta, 46, 2021–2037.

Mehta, P.K. (1987) Natural pozzolans: Supplementary cementing materials for concrete. CANMET Special Publication, 86, 1–33.

——— (1990) Concrete in the Marine Environment. Elsevier, Oxford.

Mehta, P., and Monteiro, P.J.M. (2015) Concrete: Microstructure, Properties, and Materials, 4th ed. McGraw Hill, New York.

Meier, D.C., Davis, J.M., and Vicenzi, E.P. (2011) An examination of kernite ($Na_2B_4O_6(OH)_2·3H_2O$) using X-ray and electron spectroscopies: Quantitative microanalysis of a hydrated low-Z mineral. Microscopy and Microanalysis, 17, 718–727.

Merlino, S., Bonaccorsi, E., and Armbruster, T. (2001) The real structure of 11Å tobermorite: normal and anomalous forms, OD character and polytypic modifications. European Journal of Mineralogy, 13, 577–590.

Mertens, G., Snellings, R., Van Balen, K., Bicer-Simsir, B., Verlooy, P., and Elsen, J. (2009) Pozzolanic reactions of common natural zeolites with lime and factors affecting their reactivity. Cement and Concrete Research, 39, 233–240.

Mitsuda, T., and Taylor, H.F.W. (1978) Normal and anomalous tobermorites. Mineralogical Magazine, 42, 229–235.

Myers, R.P., L'Hôpital, E., Provis, J.L., and Lothenbach, B. (2015a) Effect of temperature and aluminium on calcium (alumino)silicate hydrate chemistry under equilibrium conditions. Cement and Concrete Research, 68, 83–93.

——— (2015b) Composition–solubility–structure relationships in calcium (alkali) aluminosilicate hydrate (C-(N, K-)A-S-H). Dalton Transactions, doi:10.1039/c5dt01124h.

Oleson, J.P. (2014) Ancient literary sources concerned with Roman concrete technol-

ogy. In J.P. Oleson, Ed., Building for Eternity, p. 11–36, Oxbow Books, Oxford.

Oleson, J.P., Bottalico, L., Brandon, C., Cucitore, R., Gotti, E., and Hohlfelder, R.L. (2006) Reproducing a Roman maritime concrete structure with Vitruvian pozzolanic concrete. Journal of Roman Archaeology, 19, 29–52.

Passaglia, E., Vezzalini, G., and Carnevali, R. (1990) Diagenetic chabazites and phillipsites in Italy: crystal chemistry and genesis. European Journal of Mineralogy, 2, 827–839.

Provis, J.L., and Bernal, S.A. (2014) Geopolymers and related alkali-activated construction materials. Annual Reviews of Material Research, 44, 299–327.

Richardson, I.G. (2014) Model structures for C-(A)-S-H(I). Acta Crystallographica, B70, 903–923.

Richardson, I.G., Skibsted, J., Black, L., and Kirkpatrick, R.L. (2010) Characterisation of cement hydrate phases by TEM, NMR and Raman spectroscopy. Advances in Cement Research, 22, 233–248.

Sharma, S.K., Simons, B., and Yoder, H.S. (1982) Raman study of anorthite, calcium Tschermak's pyroxene, and gehlenite in crystalline and glassy states. American Mineralogist, 68, 1113–1125.

Sheppard, R.A., and Hay, R.L. (2001) Formation of zeolites in open hydrologic systems. Reviews in Mineralogy and Geochemistry, 45, 261–276.

Snellings, R. (2015) Surface chemistry of calcium aluminosilicate glasses. Journal of the American Ceramic Society, 98, 303–314.

Snellings, R., Mertens, G., and Elsen, J. (2012) Supplemental cementitious materials. Reviews Mineralogy Geochemistry, 74, 211–278.

Stanislao, C., Rispoli, C., Vola, G., Cappelletti, P., Morra, V., and de Gennaro, M. (2011) Contribution to the knowledge of ancient Roman seawater concretes. Phlegrean pozzolan adopted in the construction of the harbour at Soli-Pompeiopolis (Mersin, Turkey). Periodico di Mineralogia, 80, 471–488.

Tamura, N., Kunz, M., Chen, K., Celestre, R.S., MacDowell, A.A., and Warwick, T. (2009) A superbend X-ray microdiffraction beamline at the Advanced Light Source. Material Science and Engineering A, 524, 28.

Taylor, H.F.W. (1992) Tobermorite, jennite, and cement gel. Zeitschrift für Kristallographie, 202, 41–50.

Taylor, M.W., and Surdam, R.C. (1981) Zeolite reactions in the tuffaceous sediments at Teels March, Nevada. Clays and Clay Minerals, 29, 314–352.

Trotignon, L., Devallois, V., Peycelon, H., Tiffreau, C., and Bourbon, X. (2007) Predicting the long term durability of concrete engineered barriers in a geological repository for radioactive waste. Physics and Chemistry of the Earth, Parts A/B/C, 32, 259–274.

Tsuji, M., and Komarneni, S. (1989) Alkali metal ion exchange selectivity of Al-substituted tobermorite. Journal of Materials Research, 4, 698–703.

Vanorio, T., and Kanitpanyacharoen, W. (2015) Rock physics of fibrous rocks akin to Roman concrete explains uplifts at Campi Flegrei caldera. Science, 349, 617–621.

Vola, G., Gotti, E., Brandon, C., Oleson, J.P., and Hohlfelder, R.L. (2011) Chemical, mineralogical and petrographic characterization of Roman ancient hydraulic concretes cores from Santa Liberata, Italy, and Caesarea Palestinae, Israel. Periodico di Mineralogia, 80, 317–338.

Wehrmeister, U., Soldati, A.L., Jacob, D.E., Häger, T., and Hofmeister, W. (2010) Raman spectroscopy of synthetic, geological and biological vaterite a Raman spectroscopic study. Journal of Raman Spectroscopy, 41, 193–201.

Yamazaki, S., and Toraya, H. (2001) Determination of positions of zeolitic calcium atoms and water molecules in hydrothermally formed aluminum-substituted tobermorite-1.1 nm using synchrotron radiation. Journal of the American Ceramic Society, 84, 2685–2690.

Youssef, H., Ibrahim, D., Komarneni, S., and Mackenzie, K.J.D. (2010) Synthesis of 11Å Al-substituted tobermorite from trachyte rock by hydrothermal treatment. Ceramics International, 36, 203–209.

**Appendix Table 1.** Roman texts describing the geologic materials and cementitious processes of marine concrete, translations (Oleson 2014)

| | English Translation | Interpretation |
|---|---|---|
| **Vitruvius** **30–22 BCE** *de Architectura* 2.6.1 | There is a kind of powdery earth (*pulvis*) that by its nature produces wonderful results. It occurs in the neighborhood of Baiae and the territory of the municipalities around Mount Vesuvius. This material, when mixed with lime and rubble (*calce et caemento*) not only furnishes strength to other buildings, but also, when breakwaters (*moles*) are built in the sea, they set underwater… Thus, when these three substances (pumiceous ash (*pulvis*), lime (*calx*), and tuff (*tofus*)) formed in a similar manner by the strength of fire are brought together in one mixture, and suddenly they are put into contact with [sea-] water, they cohere into a single mass, quickly solidifying, hardened by the moisture, and neither the effect of the waves nor the effect of water can dissolve them. | Hydration of lime and pumiceous volcanic ash from the Campi Flegrei (and Vesuvius) volcanic districts (Fig. 2) with seawater created pozzolanic reactions that produce cementitious hydrates, mainly C-A-S-H, and rapid solidification of massive concrete structures that resisted the erosive action of seawater and the force of impact of storm waves in the marine environment. |
| **Vitruvius** **30–22 BCE** *de Architectura* 2.6.4 | Therefore, when dissimilar and incompatible materials [lime (*calx*), pumiceous ash (*pulvis*), and tuff (*tofus*)] are taken and mixed in a moist environment the urgent need of moisture suddenly satiated by [sea-] water seethes with the latent heat in these substances and causes them to gather into a unified mass and gain solidity quickly. | Exothermic heat evolved from the production of C-A-S-H binder through pozzolanic reaction of lime, pumiceous ash, and seawater led to rapid solidification of the marine concrete. |
| **Strabo** **64/63 BCE–c.24 CE** *Geographica* 5.4.6 | Puteoli has become a very great emporium because it has an artificially constructed harbor, something made possible by the natural qualities of the local sand (*ámmos*), which is well-suited to the lime and takes a firm set and solidity. Therefore, by mixing the sand-ash (*ammokonía*) with the lime, they can run moles out into the sea and in this way make the exposed shore into a protected bay, so that the largest cargo ships can anchor there safely. | In the decades following Vitruvius' descriptions of pozzolanic reaction in the marine concrete, pumiceous volcanic ash shipped from the harbor at Puteoli became a requisite component of maritime harbor construction. |
| **Seneca** **4 BCE–65 CE** *Quaestiones Naturales* 3.20.3-4 | The water is adulterated and throws a sediment (*limus*) of such a nature that it cements (*adglutinet*) and hardens objects. Just as the [volcanic ash] *Puteolanus pulvis* becomes rock (*saxum est*) if it touches water so, by contrast, if this water touches something solid it clings to it and forms concretions. | Geologic processes for calcium carbonate cements in the Hebrus River, Thrace, and in travertine deposits near Rome, are compared with hydration of *pulvis* ash to form tuff. |
| **Pliny the Elder** **23–79 CE** *Naturalis Historia* 35.166 | For who could marvel enough that on the hills of Puteoli there exists a dust (*pulvis*)—so named because it is the most insignificant part of the Earth—that, as soon as it comes into contact with the waves of the sea and is submerged, becomes a single stone mass, impregnable to the waves and every day stronger… | A geologic analog to explain rock-like cohesion in marine concrete that improves over time calls upon the hydration processes through which *pulvis* ash cements itself to form tuff. |

*Notes:* Increasing complexity in Roman construction durability and architectural design through invention, technology transfer, and competitive selection is described explicitly by Vitruvius in *de Architectura* (2.1.2, 2.1.7). Accelerated late Republican accelerated late Republican era innovations in construction engineering produced the resilient and rock-like concrete structures (Jackson and Kosso 2013). Marine concrete technologies fell into disuse about 4th C CE (Brandon et al. 2014).